Pablo A. Baier*
Departamento de Mecatrônica
Instituto Federal de Educação
Ciência e Tecnologia do Ceará
Rua Estevão Remígio 1145,
Limoeiro do Norte, CE, Brazil

Jürgen A. Baier-Saip
Departamento de Matemática
Física y Estadística
Universidad Católica del Maule
Av. San Miguel 3605,
Casilla 617, Talca, Chile

Klaus Schilling
Lehrstuhl für Informatik VII
Julius-Maximilians-Universität
Würzburg
Am Hubland, 97074 Würzburg,
Germany

Jauvane C. Oliveira
Departamento de Computação
Laboratório Nacional de
Computação Científica
Av. Getúlio Vargas 333,
Petrópolis, RJ, Brazil

Simulator for Minimally Invasive Vascular Interventions: Hardware and Software

Abstract

In the present work, a simulation system is proposed that can be used as an educational tool by physicians in training basic skills of minimally invasive vascular interventions. In order to accomplish this objective, initially the physical model of the wire proposed by Konings has been improved. As a result, a simpler and more stable method was obtained to calculate the equilibrium configuration of the wire. In addition, a geometrical method is developed to perform relaxations. It is particularly useful when the wire is hindered in the physical method because of the boundary conditions. Then a recipe is given to merge the physical and the geometrical methods, resulting in efficient relaxations. Moreover, tests have shown that the shape of the virtual wire agrees with the experiment. The proposed algorithm allows real-time executions, and furthermore, the hardware to assemble the simulator has a low cost.

1 Introduction

Over the last decades, minimally invasive surgery (MIS) has revolutionized many surgical procedures (Basdogan, De, Kim, Muniyandi, Kim, & Srinivasan, 2004). The treatment is delivered using image guidance, so that skillful instrument navigation and a thorough understanding of the anatomy are critical to avoid complications. According to Fuchs (2002), "... two major drawbacks have emerged with the introduction of MIS: firstly, the prolonged learning curve for most surgeons, in comparison to the learning process in open surgery; and secondly, increased costs due to investment in the equipment required and the use of disposable instruments ..." Since the development of MIS has a lesser sense of touch compared to open surgery, surgeons must rely more on the feeling of net forces resulting from tool–tissue interactions and, eventually, longer training is needed.

The combination of traditional learning methods and technology enhances trainee satisfaction and skill acquisition level (Engum, Jeffries, & Fisher, 2003; Tsang et al., 2008). The training methods include live observation of procedures, practicing on mechanical models, and hands-on training using human cadavers or live animals. In the past, hands-on training was considered the

Presence, *Vol. 25, No. 2, Spring 2016,* 108–128
doi:10.1162/PRES_a_00250
© *2016 by the Massachusetts Institute of Technology*

*Correspondence to pablo.baier@ifce.edu.br.

best available method (Lunderquist et al., 1995; Mori, Hatano, Maruyama, & Atomi, 1998). However, it has ethical issues and it is also expensive, owing to the costs associated with the use of animals in the process and because the instruments can be used only once (Coles, Meglan, & John, 2011).

Several training sessions can be performed with the aid of simulation techniques, providing certain levels of proficiency to the physician. Based on these findings, the U.S. Food and Drug Administration (FDA) accepted the proposal that considers a virtual reality simulator (VRS) as an important component of a training package for carotid stenting: "Trainees would learn catheter and wire-handling skills on a high-fidelity VRS until the trainees achieved a level of proficiency in didactic and technical skills" (Gallagher & Cates, 2004).

Cardiac catheterization is a minimally invasive procedure commonly used to diagnose and treat heart conditions (Balaji & Shah, 2011). During catheterization, small tubes (catheters) are inserted into the circulatory system through the femoral artery and vein as the preferred access sites (Kasper, 2015). Using X-ray fluoroscopy, information is obtained about blood flow and pressures within the heart, and it is determined if there are obstructions within the blood vessels feeding the heart muscle. For interventional procedures (e.g., stenting and balloon angioplasty), a wire (WI) must be inserted through the catheter and maneuvered in the coronaries. Achieving optimal outcomes requires operator skills in guiding the WI, as well as selecting and using the surgical tools (Moscucci, 2014).

In general, vascular simulators such as Angio Mentor by Simbionox, VIST system by Mentince and CATHIS by CATHi GmbH are expensive and complex. However, they offer advantages: no radiation is required, specific cases can be handled with multiple difficulty levels, and there are no additional costs per training session. Procedures start with a needle insertion into the vascular system, but current commercial simulators skip this step in order to reduce complexity and cost. The guidewire and the catheter are then manipulated within the vascular anatomy to navigate to the position of interest. The simulation can be used as an initial training step to develop skills before further proceeding with training in animals or humans (Alderliesten, Konings, & Niessen, 2004). Simulators are able to differentiate advanced operators from novice operators, suggesting that it is a valid tool in the assessment of performances (Tsang et al., 2008). VRS are not exclusively used for training purposes because they can be easily customized to provide both medical programs and certification boards with an objective tool for assessing physician skill and knowledge (Willaert, Aggarwal, Herzeele, Cheshire, & Vermassen, 2012).

In this work, a complete system for the simulation of minimally invasive vascular intervention is described. The environment is composed of a hardware that captures the movements of the guidewire and an algorithm that simulates the motion inside arteries. Furthermore, the commands of the C-arm (an X-ray source and image intensifier) are incorporated into the hardware.

The major contributions are as follows:

- In comparison with the paper of Konings, van de Kraats, Alderliesten, and Niessen (2003):
  - The WI model is more accurate, especially when the bending is large.
  - The update equations are simpler and the numerical calculations faster.
  - The WI segment can be introduced at once (it is not necessary to make subdivisions).
- A geometrical method is introduced, which helps to improve the speed when the WI is hindered by boundary conditions.
- A hardware device is described, which is simple to deploy and low cost. This can help to disseminate the technique and make it widespread.

2 Related Research

This work is based on the developments of Konings et al. (2003) in an analytical approximation to the problem of the guidewire. The algorithm is highly generic and has good convergence properties. It is based on quasi-static mechanics, which models the guidewire propagation without specific knowledge about friction forces. The motion is considered to be the result of a forced translation of the proximal guidewire body into

the introducer sheath, effected by the physician. The translation is a stepwise process which calculates how the guidewire reacts to an introduction of a small WI segment, giving a new steady-state position. Alderliesten, Konings, and Niessen (2007) improved the model, incorporating the friction between the guidewire and the vasculature.

The guidewire is similar to the model of the rope (knot) proposed by Brown, Latombe, and Montgomery (2004) and extended by Müller, Kim, and Chentanez (2012) to simulate hair and fur. They apply the idea based on "Follow the Leader," which is a purely geometrical technique where a chain of particles defines a curve representing a rope. Each particle moves towards its predecessor to enforce their mutual distance to be constant. The speed of the algorithm for computing the global shape of the rope saves time that can be used on the collision detection and on the management modules.

The Cosserat continuum theory of thin objects (shells, rods, and points) can be used to model the guidewire (Pai, 2002; Rubin, 2000). Cao and Tucker (2008) employed the Cosserat method to explore the nonplanar nonlinear dynamics of elastic rods. Later, Gao et al. (2015) described the dynamic behavior of the guidewire with the Lagrange equations of motion and applied the penalty method to maintain the constraints. They proposed a simplified solving procedure to integrate the resulting equations more easily.

Another method to model the deformation of a guidewire or a similar body is a representation based on the 3D beam theory (Przemieniecki, 1985). The elementary stiffness matrix relates angular and spatial positions of each end of a beam element to the applied forces and torques. Duriez, Cotin, Lenoir, and Neumann (2006) improved the accuracy and treat geometric nonlinearities, while maintaining real-time computation. They considered a Finite Element Modeling approach and developed a new mathematical representation combined with an incremental technique, that allows for highly nonlinear behavior. In particular, a new method is presented for correctly handling contact response in complex situations where a large number of nodes are subject to nonholonomic constraints.

Some simulators also include interactive fluid dynamics of blood flow, volumetric contrast agent propagation, and real-time collision detection and response (Coles et al., 2011). Current efforts are aimed towards integrating performance assessment and user guidance (Willaert et al., 2012).

One of the most time-consuming tasks in the simulation is the calculation of energy gradients in the Physical Relaxation (PR). This problem has previously been addressed (Baier, Srinivasan, Baier-Saip, Voelker, & Schilling, 2015). In particular, an efficient collision–detection algorithm was developed based on space partitioning. Furthermore, a continuous vector field (modulus and direction) was proposed, giving a realistic representation of the WI-surface interaction. On the other hand, Luboz, Blazewski, Gould, and Bello (2009) introduced a simplified deformable vascular model, but it is not smooth and contains surface irregularities which affect the collision response.

Besides the virtual model, the simulator must capture the WI motion. The hardware can be built, for example, using an optical encoder (Kodama et al., 2012) or a haptic device (Luboz et al., 2009). For instance, the Vascular Simulation Platform by Xitact is specifically designed to coaxially track a catheter and a guidewire. However, these solutions are expensive to buy or difficult to assemble.

Another promising surgery technique uses teleoperation. This technique protects the physician from X-ray radiation and solves the lack of experienced physicians in remote areas (Yu, Guo, Guo, & Shao, 2015). The slave manipulator detects the force of a catheter being inserted into the blood vessels. Then the master manipulator produces an equal damping force based on magnetorheological fluids. Since VRS is similar to teleoperation, any progress made on one front can contribute to the other one.

3 Methods

The model of Konings et al. (2003) considers the WI as a discrete set of joints at positions $\mathbf{x}_0, \ldots, \mathbf{x}_n$, with $\mathbf{x}_0$ fixed. There are n segments and the i-th segment

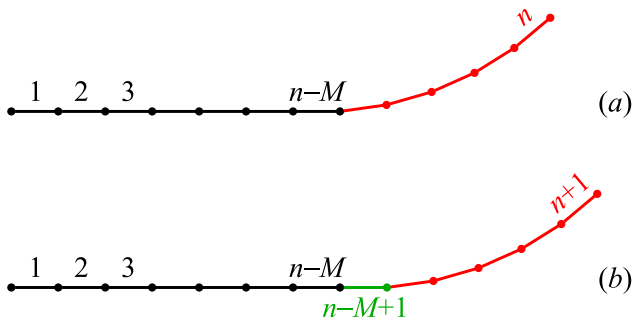

Figure 1. *(a) The WI has a curved tip (red) with M segments. They are numbered from the proximal end to the distal end of the WI. (b) The new segment (green) points to the same direction as the segment number n − M, and the total number increases to n + 1.*

$\boldsymbol{\lambda}_i = \mathbf{x}_i - \mathbf{x}_{i-1}$ is represented by a small rigid rod which is neither compressible nor bendable. Further, the size $|\boldsymbol{\lambda}_i|$ is the same for all segments (Alderliesten, Bosman, & Niessen, 2006).

When parts of the WI are inserted into the vessel, the current representation is adapted by adding segments and computing a new configuration with an optimization algorithm (relaxations). Pushing the WI into the vessel mainly affects its end, while the rest of the scene looks almost static. Hence, the natural way to add a new segment is to introduce it just before the curved tip, with the same orientation as the previous segment (see Figure 1). The WI can also be rotated but this action affects only the tip which is intrinsically curved.

In Sections 3.1 and 3.2, two different and complementary methods are explained to implement the relaxation. The combination of both methods is shown in Section 3.3. In addition, Section 3.4 presents a hardware which can be used to build this simulator.

3.1 Physical Relaxation

Figure 2 illustrates the WI geometry. Since

$$\mathbf{x}_j = \mathbf{x}_0 + \sum_{k=1}^{j} \boldsymbol{\lambda}_k ,$$

updating the i-th segment $\boldsymbol{\lambda}_i$ influences the joints from $\mathbf{x}_i$ up to $\mathbf{x}_n$. For this reason, more relaxations are needed

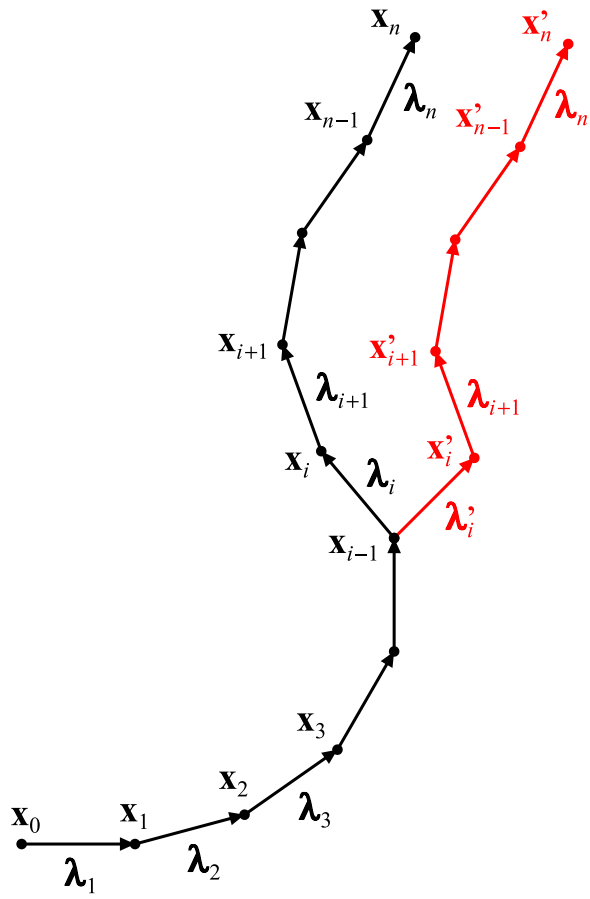

Figure 2. *The WI geometry. The difference between the coordinates of two consecutive joints $\mathbf{x}_j - \mathbf{x}_{j-1}$ is equal to the vector $\boldsymbol{\lambda}_j$, which has a constant length λ. Changing $\boldsymbol{\lambda}_i$ modifies only $\mathbf{x}_i, \mathbf{x}_{i+1}, \ldots, \mathbf{x}_{n-1}, \mathbf{x}_n$, and the difference between the new and the old coordinates $\mathbf{x}'_j - \mathbf{x}_j = \boldsymbol{\lambda}'_i - \boldsymbol{\lambda}_i$ is the same for $j = i, i+1, \cdots, n-1, n$.*

close to the distal end of the WI. A PR cycle is defined to be the sequence of n iterations

iteration 1: update segment n,
iteration 2: update segments $n, n-1$,
iteration 3: update segments $n, n-1, n-2$,
$\vdots$
iteration n: update segments $n, n-1, \ldots, 2, 1$.

The algorithm of Konings et al. (2003) also proceeds from the distal end to the proximal end. The total number of updates in one cycle equals $\frac{1}{2}n(n+1)$.

To ensure numerical stability, every time an "action" is performed (add a segment, remove a segment, or rotate the WI) a Tip Relaxation is executed:

1. A number of $\frac{1}{2}m(m+1)$ updates (corresponding to the first m iterations) is carried out. Thus, the m segments closest to the tip are always updated. Since the actions take place just before the curved tip (see Figure 1), m is chosen as $M+5$ to ensure that all affected segments will be updated at least five times before a new action is performed. However, if the WI is very stiff, then it is necessary to replace 5 by a bigger number.
2. Additionally, one update is executed for the segment numbers $n-m-5, n-m-10, n-m-15, \ldots$ up to the proximal end of the WI. This ensures some degree of relaxation besides the tip. Otherwise, if a large number of actions is performed in a short time interval, the rest of the WI would be far away from equilibrium.

The numerical performance can be increased if incomplete cycles are carried out; that is, some of the last iterations (Alderliesten et al., 2007) are suppressed. In what follows, the physical model of the WI is improved and an updating recipe is given, which is simpler to apply than the recipe of Konings et al. (2003).

3.1.1 Bending Energy. Consider the bending energy U_i of a WI segment (an arc) defined by three points $\mathbf{x}_{i-1}, \mathbf{x}_i$, and $\mathbf{x}_{i+1}$ (see Figure 3)

$$U_i = \frac{1}{2}\frac{EI_i}{R_i^2}s_i\,, \tag{1}$$

where EI_i represents the flexural rigidity, R_i is the radius, and $s_i = R_i\theta_i$ is the arc length between $\mathbf{x}_{i-1}$ and $\mathbf{x}_i$ (or equivalently between $\mathbf{x}_i$ and $\mathbf{x}_{i+1}$). Note that U_i does not represent the elastic energy between the points $\mathbf{x}_{i-1}$ and $\mathbf{x}_{i+1}$, but only half of this arc.

From Figure 3 it follows that the distance between two points is given by $\lambda = 2R_i\sin(\theta_i/2)$. Hence Equation 1 can be put in the form

$$U_i = \frac{EI_i}{2R_i}\theta_i = \frac{EI_i}{\lambda}\theta_i\sin\frac{\theta_i}{2}\,. \tag{2}$$

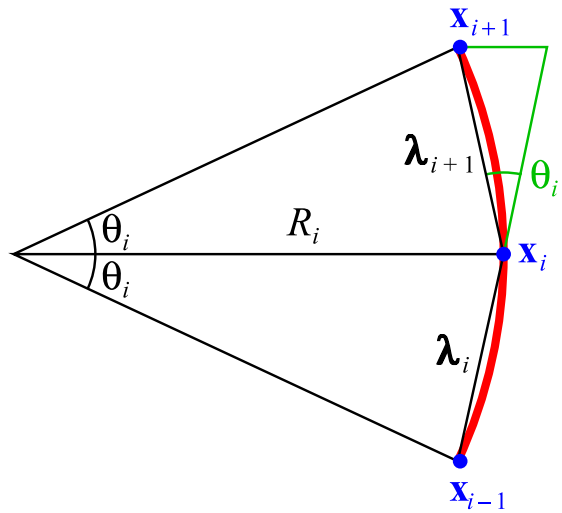

Figure 3. *Three successive points $\mathbf{x}_{i-1}$, $\mathbf{x}_i$, and $\mathbf{x}_{i+1}$ separated by an equal distance $\lambda = |\boldsymbol{\lambda}_i| = |\boldsymbol{\lambda}_{i+1}|$ define a circular arc of radius R_i and angle $2\theta_i$.*

For $\theta_i \ll 1$ the last equation reduces to Equation 3 of Alderliesten et al. (2004)

$$U_i = \frac{1}{2}\frac{EI_i}{\lambda}\theta_i^2\,.$$

The angle θ_i can be calculated using the formula $\cos\theta_i = \boldsymbol{\lambda}_i.\boldsymbol{\lambda}_{i+1}/\lambda^2$. If the WI is intrinsically curved at joint i, then $\boldsymbol{\lambda}_{i+1}$ must be replaced by $\mathbf{x}_{i+1} - \mathbf{x}_i - \boldsymbol{\omega}_{i+1}$ (see Figure 4). Further, rotating the WI changes the orientation of $\boldsymbol{\omega}_{i+1}$. Since

$$\theta\sin\frac{\theta}{2} \approx (1-\cos\theta) + \frac{1}{12}(1-\cos\theta)^2 + \frac{3}{1280}\theta^6\,, \tag{3}$$

up to fourth order in θ_i

$$\begin{aligned} U_i(\boldsymbol{\lambda}_i, \boldsymbol{\lambda}_{i+1}) &= \frac{EI_i}{12\lambda}\left[13 - 14\cos\theta_i + \cos^2\theta_i\right] \\ &= \frac{C_i}{12}\left[13 - 14\frac{\boldsymbol{\lambda}_i.\boldsymbol{\lambda}_{i+1}}{\lambda^2} + \frac{(\boldsymbol{\lambda}_i.\boldsymbol{\lambda}_{i+1})^2}{\lambda^4}\right], \end{aligned} \tag{4}$$

where $C_i = EI_i/\lambda$ is a spring constant.

3.1.2 Energy Minimization. The orientation of the i-th segment is updated ($\boldsymbol{\lambda}_i \to \boldsymbol{\lambda}_i + \boldsymbol{\alpha}_i$) while the others $\boldsymbol{\lambda}_j$ are kept constant, in such a way that the energy decreases. The energy variation of

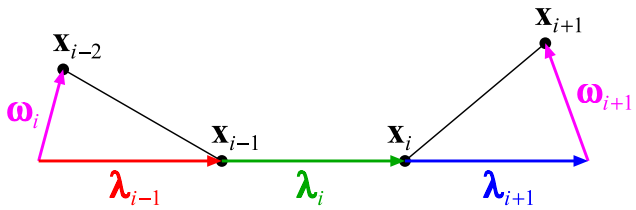

Figure 4. *The minimum energy of a WI without external forces results when $\boldsymbol{\lambda}_{i-1}$ is parallel to $\boldsymbol{\lambda}_i$, and $\boldsymbol{\lambda}_i$ is parallel to $\boldsymbol{\lambda}_{i+1}$. If $\boldsymbol{\lambda}_{i-1} = \boldsymbol{x}_{i-1} - \boldsymbol{x}_{i-2} + \boldsymbol{\omega}_i$, $\boldsymbol{\lambda}_i = \boldsymbol{x}_i - \boldsymbol{x}_{i-1}$, and $\boldsymbol{\lambda}_{i+1} = \boldsymbol{x}_{i+1} - \boldsymbol{x}_i - \boldsymbol{\omega}_{i+1}$; then the equilibrium is obtained when $\boldsymbol{x}_{i-2}$, $\boldsymbol{x}_{i-1}$, $\boldsymbol{x}_i$, and $\boldsymbol{x}_{i+1}$ are in the positions indicated. Thus, the vectors $\boldsymbol{\omega}_i$ bend a free WI.*

$U_i(\boldsymbol{\lambda}_i + \boldsymbol{\alpha}_i, \boldsymbol{\lambda}_{i+1})$ around the new position $\boldsymbol{\lambda}_i + \boldsymbol{\alpha}_i \to \boldsymbol{\lambda}_i + \boldsymbol{\alpha}_i + \delta\boldsymbol{\alpha}_i$ is up to first order

$$\delta U_i(\boldsymbol{\lambda}_i + \boldsymbol{\alpha}_i, \boldsymbol{\lambda}_{i+1}) = \frac{C_i}{6\lambda^2}\left[-7 + \frac{\boldsymbol{\lambda}_{i+1}.\boldsymbol{\lambda}_i + \boldsymbol{\lambda}_{i+1}.\boldsymbol{\alpha}_i}{\lambda^2}\right]\boldsymbol{\lambda}_{i+1}.\delta\boldsymbol{\alpha}_i\,. \quad (5a)$$

Furthermore, U_{i-1} also varies

$$\delta U_{i-1}(\boldsymbol{\lambda}_{i-1}, \boldsymbol{\lambda}_i + \boldsymbol{\alpha}_i) = \frac{C_i}{6\lambda^2}\left[-7 + \frac{\boldsymbol{\lambda}_{i-1}.\boldsymbol{\lambda}_i + \boldsymbol{\lambda}_{i-1}.\boldsymbol{\alpha}_i}{\lambda^2}\right]\boldsymbol{\lambda}_{i-1}.\delta\boldsymbol{\alpha}_i\,. \quad (5b)$$

Similarly, if the WI is intrinsically curved at joint $i-1$, then $\boldsymbol{\lambda}_{i-1}$ must be replaced by $\mathbf{x}_{i-1} - \mathbf{x}_{i-2} + \boldsymbol{\omega}_i$ (see Figure 4).

It is convenient to introduce the vectors $\hat{\mathbf{u}}_i$, $\boldsymbol{\eta}_i$, $\boldsymbol{\varepsilon}_i$, and the scalar κ_i defined by

$$\begin{aligned} \hat{\mathbf{u}}_i &= \boldsymbol{\lambda}_i/\lambda \\ \boldsymbol{\eta}_i &= \hat{\mathbf{u}}_{i-1} - \hat{\mathbf{u}}_i \\ \boldsymbol{\varepsilon}_i &= \hat{\mathbf{u}}_{i+1} - \hat{\mathbf{u}}_i \\ \kappa_i &= \hat{\mathbf{u}}_i.\hat{\mathbf{u}}_{i+1}\,. \end{aligned} \quad (6)$$

The elastic energy variation of the WI is the sum of Equations 5a and 5b

$$\delta U_{\text{elas}} = -\frac{C_i}{\lambda}\left[(p_i + q_i)\hat{\mathbf{u}}_i + p_i\boldsymbol{\eta}_i + q_i\boldsymbol{\varepsilon}_i\right].\delta\boldsymbol{\alpha}_i\,, \quad (7)$$

with

$$\begin{aligned} p_i &= \frac{1}{6}\left[7 - \kappa_{i-1} - (\hat{\mathbf{u}}_i + \boldsymbol{\eta}_i).\frac{\boldsymbol{\alpha}_i}{\lambda}\right] \approx \frac{7 - \kappa_{i-1}}{6} \\ q_i &= \frac{1}{6}\left[7 - \kappa_i - (\hat{\mathbf{u}}_i + \boldsymbol{\varepsilon}_i).\frac{\boldsymbol{\alpha}_i}{\lambda}\right] \approx \frac{7 - \kappa_i}{6}\,, \end{aligned} \quad (8)$$

because $\kappa_i \lesssim 1$ and $|\boldsymbol{\alpha}_i| \ll \lambda$ for small corrections (i.e., nearby equilibrium).

Usually, the artery deformations caused by the WI are tiny (Takashima et al., 2014), so that close to equilibrium the relation between stress and strain is linear. Changing $\boldsymbol{\lambda}_i + \boldsymbol{\alpha}_i$ by $\delta\boldsymbol{\alpha}_i$ affects the coordinates $\mathbf{x}_i, \cdots, \mathbf{x}_n$ by the same amount. Hence, due to the interactions between the WI and the artery, the surface energy also varies $\delta U_{\text{surf}} = \mathbf{G}_i.\delta\boldsymbol{\alpha}_i$. Here $\mathbf{G}_i$ stands for the sum of the gradients from joint i up to the distal end of the WI (Alderliesten et al., 2004)

$$\mathbf{G}_i = \sum_{j=i}^{n} \nabla_j\, U_{\text{surf}}(\mathbf{x}_j)\,, \quad (9)$$

where $U_{\text{surf}}(\mathbf{x}_j)$ represents energy interaction of joint j with the artery's surface.

The total energy variation is

$$\begin{aligned} \delta U &= \left[-\frac{C_i}{\lambda}(p_i + q_i)\hat{\mathbf{u}}_i - \frac{C_i}{\lambda}(p_i\boldsymbol{\eta}_i + q_i\boldsymbol{\varepsilon}_i) + \mathbf{G}_i\right].\delta\boldsymbol{\alpha}_i \\ &= \left[(B_{\mathbf{u}i} - \rho_i)\hat{\mathbf{u}}_i + B_{\mathbf{v}i}\hat{\mathbf{v}}_i + B_{\mathbf{w}i}\hat{\mathbf{w}}_i\right].\delta\boldsymbol{\alpha}_i\,, \end{aligned} \quad (10)$$

where $\hat{\mathbf{v}}_i$ and $\hat{\mathbf{w}}_i$ are two unit vectors perpendicular to $\hat{\mathbf{u}}_i$, i.e. the set $\{\hat{\mathbf{u}}_i, \hat{\mathbf{v}}_i, \hat{\mathbf{w}}_i\}$ forms an orthonormal basis with $\hat{\mathbf{u}}_i$ parallel to $\boldsymbol{\lambda}_i$. Furthermore,

$$\begin{aligned} \rho_i &= \frac{C_i}{\lambda}(p_i + q_i) \\ \mathbf{B}_i &= \mathbf{G}_i - \frac{C_i}{\lambda}(p_i\boldsymbol{\eta}_i + q_i\boldsymbol{\varepsilon}_i)\,, \end{aligned} \quad (10')$$

and $B_{\mathbf{u}i} = \mathbf{B}_i.\hat{\mathbf{u}}_i$, $B_{\mathbf{v}i} = \mathbf{B}_i.\hat{\mathbf{v}}_i$, $B_{\mathbf{w}i} = \mathbf{B}_i.\hat{\mathbf{w}}_i$.

Since the modulus of $\boldsymbol{\lambda}_i + \boldsymbol{\alpha}_i$ remains constant, it follows that $|\boldsymbol{\lambda}_i + \boldsymbol{\alpha}_i|^2 = \lambda^2$ or $2\boldsymbol{\lambda}_i.\boldsymbol{\alpha}_i = -|\boldsymbol{\alpha}_i|^2$. Thus, $\boldsymbol{\alpha}_i$ can be written in the form (see Figure 5)

$$\boldsymbol{\alpha}_i = -\frac{a_i^2}{2\lambda}\hat{\mathbf{u}}_i + H(a_i)(\cos\psi_i\hat{\mathbf{v}}_i + \sin\psi_i\hat{\mathbf{w}}_i)\,, \quad (11)$$

with

$$H(a_i) = \frac{a_i}{2\lambda}\sqrt{4\lambda^2 - a_i^2}\,. \quad (11')$$

Any variation of $\boldsymbol{\alpha}_i$ can be expressed using the parameters a_i and ψ_i

$$\begin{aligned} \delta\boldsymbol{\alpha}_i = &\left[-\frac{a_i}{\lambda}\hat{\mathbf{u}}_i + \frac{\mathrm{d}H}{\mathrm{d}a_i}(\cos\psi_i\hat{\mathbf{v}}_i + \sin\psi_i\hat{\mathbf{w}}_i)\right]\delta a_i \\ &+ H(a_i)(-\sin\psi_i\hat{\mathbf{v}}_i + \cos\psi_i\hat{\mathbf{w}}_i)\,\delta\psi_i\,. \end{aligned} \quad (12)$$

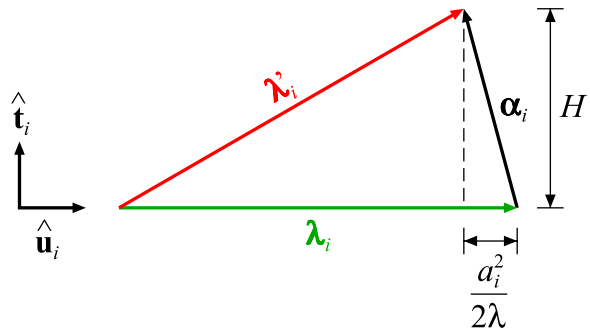

Figure 5. *The lengths of the vectors $\boldsymbol{\lambda}_i$ (old), $\boldsymbol{\lambda}'_i$ (new) are equal, and the modulus of $\boldsymbol{\alpha}_i = \boldsymbol{\lambda}'_i - \boldsymbol{\lambda}_i$ is a_i. Further, the unit vector $\hat{\mathbf{u}}_i$ is parallel to $\boldsymbol{\lambda}_i$ and perpendicular to $\hat{\mathbf{t}}_i = \cos\psi_i\hat{\mathbf{v}}_i + \sin\psi_i\hat{\mathbf{w}}_i$, where ψ_i represents the azimuthal angle of $\boldsymbol{\alpha}_i$ around $\boldsymbol{\lambda}_i$.*

At the minimum, $\delta U = 0$ for arbitrary δa_i and $\delta\psi_i$. Considering first the case $\delta a_i = 0$ and $\delta\psi_i \neq 0$

$$\left[-B_{\mathbf{v}i}\sin\psi_i + B_{\mathbf{w}i}\cos\psi_i\right]H(a_i)\,\delta\psi_i = 0\,,$$

from which it is deduced that $B_{\mathbf{w}i}\cos\psi_i = B_{\mathbf{v}i}\sin\psi_i$. Hence

$$\cos\psi_i\hat{\mathbf{v}}_i + \sin\psi_i\hat{\mathbf{w}}_i = \frac{B_{\mathbf{v}i}\hat{\mathbf{v}}_i + B_{\mathbf{w}i}\hat{\mathbf{w}}_i}{\sqrt{B_{\mathbf{v}i}^2 + B_{\mathbf{w}i}^2}}\,. \tag{13}$$

Now, the case $\delta a_i \neq 0$ and $\delta\psi_i = 0$ is examined. From Equation 11′

$$\frac{\mathrm{d}H}{\mathrm{d}a_i} = \frac{\mathrm{d}}{\mathrm{d}a_i}\left(a_i - \frac{a_i^3}{8\lambda^2} + \cdots\right) = 1 - \frac{3a_i^2}{8\lambda^2} + \cdots\,,$$

so that up to first order in a_i/λ Equation 12 becomes

$$\delta\boldsymbol{\alpha}_i = \left[-\frac{a_i}{\lambda}\hat{\mathbf{u}}_i + \frac{B_{\mathbf{v}i}\hat{\mathbf{v}}_i + B_{\mathbf{w}i}\hat{\mathbf{w}}_i}{\sqrt{B_{\mathbf{v}i}^2 + B_{\mathbf{w}i}^2}}\right]\delta a_i\,,$$

where Equation 13 has been used. Therefore Equation 10 gives

$$\left[-\frac{a_i}{\lambda}(B_{\mathbf{u}i} - \rho_i) + \sqrt{B_{\mathbf{v}i}^2 + B_{\mathbf{w}i}^2}\right]\delta a_i = 0 \tag{14}$$

and solving

$$a_i = \lambda\frac{\sqrt{B_{\mathbf{v}i}^2 + B_{\mathbf{w}i}^2}}{B_{\mathbf{u}i} - \rho_i}\,. \tag{15}$$

Note that changing the sign of Equation 13, as in the work of Alderliesten et al. (2004), also changes the sign of a_i in the last equation. Since $H(a_i)$ is an odd function, the product $H(a_i)\,(\cos\psi_i\hat{\mathbf{v}}_i + \sin\psi_i\hat{\mathbf{w}}_i)$ is the same irrespective of the chosen sign.

3.1.3 First Order Correction. Because the norm of the vector $\boldsymbol{\lambda}_i$ remains constant, only the change of direction needs to be updated in the calculations: $\hat{\mathbf{u}}_i \to \hat{\mathbf{u}}_i + \Delta\hat{\mathbf{u}}_i = \hat{\mathbf{u}}_i + \boldsymbol{\alpha}_i/\lambda$. In particular, note that for $a_i \ll \lambda$ Equation 11 becomes

$$\boldsymbol{\alpha}_i \approx a_i(\cos\psi_i\hat{\mathbf{v}}_i + \sin\psi_i\hat{\mathbf{w}}_i) = \lambda\frac{B_{\mathbf{v}i}\hat{\mathbf{v}}_i + B_{\mathbf{w}i}\hat{\mathbf{w}}_i}{B_{\mathbf{u}i} - \rho_i}$$

or

$$\Delta\hat{\mathbf{u}}_i = \frac{\boldsymbol{\alpha}_i}{\lambda} \approx -\frac{\hat{\mathbf{u}}_i \times (\mathbf{B}_i \times \hat{\mathbf{u}}_i)}{\rho_i - \hat{\mathbf{u}}_i.\mathbf{B}_i}\,. \tag{16}$$

The scalar $\hat{\mathbf{u}}_i.\mathbf{B}_i = B_{i\|}$ is the projection of $\mathbf{B}_i$ along $\hat{\mathbf{u}}_i$ and $\hat{\mathbf{u}}_i \times (\mathbf{B}_i \times \hat{\mathbf{u}}_i) = \mathbf{B}_i - \hat{\mathbf{u}}_i(\hat{\mathbf{u}}_i.\mathbf{B}_i) = \mathbf{B}_i - \mathbf{B}_{i\|} = \mathbf{B}_{i\perp}$ represents the component of $\mathbf{B}_i$ perpendicular to $\hat{\mathbf{u}}_i$ (the infinitesimal variation of a vector with a constant modulus is perpendicular to the vector). Since $\Delta\hat{\mathbf{u}}_i$ is only an approximation, after updating $\hat{\mathbf{u}}_i$ a renormalization must be performed.

Mostly $\hat{\mathbf{u}}_i.\mathbf{B}_i \ll \rho_i \sim 2C_i/\lambda$, so that from Equation 16

$$\Delta\hat{\mathbf{u}}_i \approx -\frac{\hat{\mathbf{u}}_i \times (\mathbf{B}_i \times \hat{\mathbf{u}}_i)}{\rho_i}\,. \tag{17}$$

As ρ_i is nearly constant, to achieve equilibrium ($\Delta\hat{\mathbf{u}}_i \to 0$) the component of $\hat{\mathbf{u}}_i$ perpendicular to $\mathbf{B}_i$ must be minimized. Notice that $\mathbf{B}_i$ depends on $\mathbf{G}_i$, so that the calculation of $\mathbf{G}_i$ plays a crucial role.

Suppose that all updates $\Delta\hat{\mathbf{u}}_i$ have nearly the same magnitude and are randomly oriented. As in random walks, the average distance covered by the tip when the segments between i and n are updated is proportional to $\sqrt{n+1-i}$. Thus $|\mathbf{x}_{n,\mathrm{new}} - \mathbf{x}_{n,\mathrm{old}}|$ can become very large. To avoid this unstable behavior, the update is bounded using the formula

$$|\Delta\hat{\mathbf{u}}_i| \leq \frac{\Delta u_{\max}}{\sqrt{n+1-i}}\,, \tag{18}$$

where $i = 1, \cdots, n$ and $\Delta u_{\max}$ is small ($\sim$0.1). In a frontal collision of the WI with the surface, a single update can bend the tip at most by the amount $\Delta u_{\max}$. When the calculation proceeds, the next iterations will

bend the tip further until $|\Delta\hat{\mathbf{u}}_i|$ naturally decreases and the WI approaches equilibrium.

The updates $\Delta\hat{\mathbf{u}}_i$ for small i are tiny because they are bounded by Equation 18. Hence, instabilities are dissipated and do not propagate to the proximal end of the WI. It is the tip of the WI (i close to n) which plays an important role in the simulation and, in this region, a higher number of updates is performed. Since the relaxation is stable, there is no need to introduce the segment in small steps as in the work of Alderliesten et al. (2004), and it can be performed at once.

If $|\mathbf{B}_i| \ll \rho_i$, the update will be small. In this case, the denominator in Equation 16 is positive and the update moves the WI in a direction so as to cancel $\mathbf{B}_i$. But in a frontal collision of the tip with the artery, $\mathbf{B}_i$ can become very large because of $\mathbf{G}_i$. If the sign of the denominator is negative, $\mathbf{B}_i$ will increase instead of canceling, and the calculations diverge. In particular, for $\rho_i - \hat{\mathbf{u}}_i.\mathbf{B}_i \approx 0$ the modulus $|\boldsymbol{\alpha}_i|$ becomes larger than 2λ, which is geometrically impossible. In such cases, the approximation $\mathrm{d}H/\mathrm{d}a_i = 1$ fails.

To overcome this drawback, Equation 14 should be considered without approximations

$$-\frac{a_i}{\lambda}(B_{\mathbf{u}i} - \rho_i) + \frac{2\lambda^2 - a_i^2}{\lambda\sqrt{4\lambda^2 - a_i^2}}\sqrt{B_{\mathbf{v}i}^2 + B_{\mathbf{w}i}^2} = 0,$$

and solve numerically for a_i. However, a simple estimation for $\Delta\hat{\mathbf{u}}_i$ can be found. Taking the absolute value in the denominator of Equation 16

$$\Delta\hat{\mathbf{u}}_i = -\frac{\hat{\mathbf{u}}_i \times (\mathbf{B}_i \times \hat{\mathbf{u}}_i)}{|\rho_i - \hat{\mathbf{u}}_i.\mathbf{B}_i|}, \tag{19}$$

the update will always be in the right direction. Note that using Equation 17 in place of Equation 19 gives similar results. The magnitude of the correction can still be large, but since $|\Delta\hat{\mathbf{u}}_i|$ is bounded and $\hat{\mathbf{u}}_i$ is renormalized after each update, it poses no problem. Applying Equations 18 and 19 in the Tip Relaxation results in a stable algorithm, even if in a short time interval, a large number of actions are performed by the user.

Lastly, it is observed that Equation 19 basically involves the calculation of $\mathbf{B}_i$ and the computation of scalar and cross products with $\hat{\mathbf{u}}_i$. On the other hand, Equation 11 of Alderliesten et al. (2004) works implicitly with an orthonormal basis. It is necessary to calculate the projections of $\mathbf{B}_i$ in this base, to determine the modulus a_i, the angle ψ_i, and then to construct the vector $\boldsymbol{\alpha}_i$ again using the base. Thus, the method developed in this work is simpler to apply.

3.1.4 Pseudocode.

```
void PhysicalUpdate(segment i){
    1. calculate the gradient G_i, see Equation 9;
    2. calculate the update Δû_i, see Equations 18
    and 19;
    3. update û_i and renormalize;
    4. update x_i, x_{i+1}, ···, x_n;
    5. update ω_i, ω_{i+1}, ···, ω_n;
}
```

The function `PhysicalUpdate` implements the method described in this section. Next, the processing time (PT) spent in calling the function during a complete PR cycle is analyzed.

For a segment number i, the calculation of $\mathbf{G}_i$ involves the collision test for $n - i$ segments. During the cycle of the PR, this function is called $\frac{1}{2}n(n+1)$ times, and the total number of collision tests in one cycle is $\frac{1}{6}n(n+1)(n+2)$. If there is a collision for $j > i$, then $\nabla_j U_{\mathrm{surf}}(\mathbf{x}_j)$ must be calculated. The number of times the gradient is computed depends on j. For example, if $j = n/2$ the computation is repeated $\frac{1}{8}n(n+2) \approx n^2/8$ times, and in general it will be a fraction of n^2. Thus, the PT of line **1** has the form $\frac{1}{6}n(n+1)(n+2)T_1 + n^2 T_2$, where T_1 and T_2 are positive constants.

The lines **2** and **3** involve a single execution, so that the PT of one cycle is proportional to $\frac{1}{2}n(n+1)$. Finally, lines **4** and **5** give a contribution similar to the number of collision tests executed, i.e. proportional to $\frac{1}{6}n(n+1)(n+2)$. Hence, the estimated PT of the physical update cycle is

$$\begin{aligned} t_{\mathrm{phy}} &= t_{\mathrm{p1}}n + t_{\mathrm{p2}}n^2 + t_{\mathrm{p3}}n^3 \\ &\approx t_{\mathrm{p2}}n^2 + t_{\mathrm{p3}}n^3 . \end{aligned} \tag{20}$$

In the last line, the PT is approximated by the two main contributions for large n.

Since Tip Relaxation plays a central role in the algorithm, its PT will also be examined. In the first part, when the first m segments are updated, the PT is similar to Equation 20 but with $n \to m = M + 5$ (a constant). In the second part, when the segment numbers $n - m - 5, n - m - 10, n - m - 15, \cdots$ are updated once, instead of $\frac{1}{2}n(n+1)$ only $\sim (n-m)/5$ steps are executed. Hence, for large n the term $n^2/2$ must be replaced by $n/5$ in Equation 20. The overall result is

$$t_{\text{tip}} \approx t_{\text{p1}} m + t_{\text{p2}} m^2 + t_{\text{p3}} m^3 + t_{\text{p3}} \left(\frac{2n}{5}\right)^{3/2}$$
$$= \text{const} + t_{\text{p4}} n^{3/2} . \tag{21}$$

For example, if $m = 5 + 5$ and $n = 250$, then $m^3 = 1000 = (2n/5)^{3/2}$, that is, the constant has the same order of magnitude as the last term in Equation 21.

3.2 Geometrical Relaxation

Consider the problem of finding the minimum energy of a homogeneous WI ($EI = \text{const}$) with the following boundary conditions. The end points $\mathbf{x}_\mu$ and $\mathbf{x}_\nu$ are fixed as well as the tangent vectors to the trajectory $\dot{\mathbf{x}}_\mu$ and $\dot{\mathbf{x}}_\nu$ (the dot denotes differentiation with respect to the curve parameter τ). Between these points there is no contact with the surface and the total length of the curve is not fixed.

3.2.1 Bending Energy. Here, it is necessary to derive a generalization of Equation 2 when the modulus $\lambda_i = |\boldsymbol{\lambda}_i|$ is variable. In Figure 6 the three points $\mathbf{x}_{i-1}$, $\mathbf{x}_i$, and $\mathbf{x}_{i+1}$ are joined by two arcs having the same angle θ_i but different radii R_i and R_{i+1}. It is also possible to join the points using the same radius and different angles, but the calculations become cumbersome. The sum of the energies in half arc under and in half arc above the point $\mathbf{x}_i$ is

$$U_i = \frac{1}{2}\frac{EI}{R_i^2}\frac{s_i}{2} + \frac{1}{2}\frac{EI}{R_{i+1}^2}\frac{s_{i+1}}{2}$$
$$= \frac{EI}{2}\left(\frac{\theta_i}{2R_i} + \frac{\theta_i}{2R_{i+1}}\right)$$
$$= \frac{EI}{2}\left(\frac{1}{\lambda_i} + \frac{1}{\lambda_{i+1}}\right)\theta_i \sin\frac{\theta_i}{2} ,$$

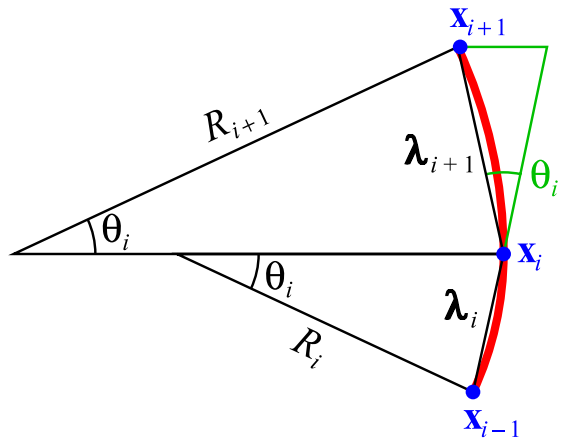

Figure 6. *Three points $\mathbf{x}_{i-1}$, $\mathbf{x}_i$, and $\mathbf{x}_{i+1}$ are separated by different distances $|\boldsymbol{\lambda}_i| \neq |\boldsymbol{\lambda}_{i+1}|$. The two circular arcs have the same angle θ_i but the radii R_i and R_{i+1} are not equal.*

because $\sin(\theta_i/2) = \lambda_i/2R_i = \lambda_{i+1}/2R_{i+1}$. Using Equation 3 with $\cos\theta_i = \hat{\mathbf{u}}_i.\hat{\mathbf{u}}_{i+1}$ results in

$$U_i = \frac{EI}{12}\left(\frac{1}{\lambda_i} + \frac{1}{\lambda_{i+1}}\right)\frac{13 - 14\,\hat{\mathbf{u}}_i.\hat{\mathbf{u}}_{i+1} + (\hat{\mathbf{u}}_i.\hat{\mathbf{u}}_{i+1})^2}{2} .$$

3.2.2 Energy Minimization. Since only $\boldsymbol{\lambda}_i$ and $\boldsymbol{\lambda}_{i+1}$ are functions of $\mathbf{x}_i$, it follows that U_{i-1}, U_i, and U_{i+1} depend on this coordinate. Omitting the constant multiplicative factor $EI/12$, it suffices to analyze the function

$$\Psi(\mathbf{x}_i) = \left(\frac{1}{\lambda_{i-1}} + \frac{1}{\lambda_i}\right)\frac{13 - 14\,\kappa_{i-1} + \kappa_{i-1}^2}{2}$$
$$+ \left(\frac{1}{\lambda_i} + \frac{1}{\lambda_{i+1}}\right)\frac{13 - 14\,\kappa_i + \kappa_i^2}{2}$$
$$+ \left(\frac{1}{\lambda_{i+1}} + \frac{1}{\lambda_{i+2}}\right)\frac{13 - 14\,\kappa_{i+1} + \kappa_{i+1}^2}{2} . \tag{22}$$

Notice that Ψ does not contain any physical parameter and depends solely on the geometry.

The label * will be used to refer to the coordinates of the improved curve. In order to minimize Ψ, substitute $\mathbf{x}_i^*$ by $\mathbf{x}_i^* + y_i\hat{\mathbf{y}}_i + z_i\hat{\mathbf{z}}_i$, where $\hat{\mathbf{y}}_i$ and $\hat{\mathbf{z}}_i$ are orthogonal to the vector $\mathbf{x}_{i+1} - \mathbf{x}_{i-1}$. The calculation of y_i and z_i can be carried out using the Hessian matrix and the gradient

$$\begin{pmatrix} \Psi_{yy,i} & \Psi_{yz,i} \\ \Psi_{yz,i} & \Psi_{zz,i} \end{pmatrix}\begin{pmatrix} y_i \\ z_i \end{pmatrix} = -\begin{pmatrix} \hat{\mathbf{y}}_i.\nabla_i\Psi \\ \hat{\mathbf{z}}_i.\nabla_i\Psi \end{pmatrix} . \tag{23}$$

The Hessian matrix gives essentially a *metric* to find the length of the update $|\mathbf{x}^*_{i,\text{new}} - \mathbf{x}^*_{i,\text{old}}|$ in the direction of steepest descent. This direction is determined by the negative components of the gradient in the plane defined by $\hat{\mathbf{y}}_i$ and $\hat{\mathbf{z}}_i$. Near the minimum, the Hessian approaches a constant. Thus, the matrix elements can be computed numerically

$$\Psi_{yy,i} = \frac{1}{(\delta\lambda)^2}\left[\Psi(\mathbf{x}^*_i + \delta\lambda\hat{\mathbf{y}}_i) - 2\Psi(\mathbf{x}^*_i) + \Psi(\mathbf{x}^*_i - \delta\lambda\,\hat{\mathbf{y}}_i)\right]$$

$$\begin{aligned}\Psi_{yz,i} = \frac{1}{4(\delta\lambda)^2}\big[\,&\Psi(\mathbf{x}^*_i + \delta\lambda\,\hat{\mathbf{y}}_i + \delta\lambda\,\hat{\mathbf{z}}_i)\\ &- \Psi(\mathbf{x}^*_i + \delta\lambda\,\hat{\mathbf{y}}_i - \delta\lambda\,\hat{\mathbf{z}}_i)\\ &- \Psi(\mathbf{x}^*_i - \delta\lambda\,\hat{\mathbf{y}}_i + \delta\lambda\,\hat{\mathbf{z}}_i)\\ &+ \Psi(\mathbf{x}^*_i - \delta\lambda\,\hat{\mathbf{y}}_i - \delta\lambda\,\hat{\mathbf{z}}_i)\big]\end{aligned}$$

$$\Psi_{zz,i} = \frac{1}{(\delta\lambda)^2}\left[\Psi(\mathbf{x}^*_i + \delta\lambda\hat{\mathbf{z}}_i) - 2\Psi(\mathbf{x}^*_i) + \Psi(\mathbf{x}^*_i - \delta\lambda\,\hat{\mathbf{z}}_i)\right], \tag{23a}$$

where $\delta\lambda = \lambda/10^4$ for calculations performed with double precision.

On the other hand, the gradient is very sensitive to numerical round off errors near the minimum. Hence $\nabla_i\Psi$ must be determined analytically with the help of $\nabla_i\lambda^*_{i-1} = \mathbf{0}$, $\nabla_i\lambda^*_i = \hat{\mathbf{u}}^*_i$, $\nabla_i\lambda^*_{i+1} = -\hat{\mathbf{u}}^*_{i+1}$, $\nabla_i\lambda^*_{i+2} = \mathbf{0}$, and

$$\begin{aligned}\nabla_i\kappa^*_{i-1} &= \frac{\hat{\mathbf{u}}^*_{i-1} - \kappa^*_{i-1}\hat{\mathbf{u}}^*_i}{\lambda^*_i}\\ \nabla_i\kappa^*_i &= \frac{\hat{\mathbf{u}}^*_{i+1} - \kappa^*_i\hat{\mathbf{u}}^*_i}{\lambda^*_i} - \frac{\hat{\mathbf{u}}^*_i - \kappa^*_i\hat{\mathbf{u}}^*_{i+1}}{\lambda^*_{i+1}}\\ \nabla_i\kappa^*_{i+1} &= -\frac{\hat{\mathbf{u}}^*_{i+2} - \kappa^*_{i+1}\hat{\mathbf{u}}^*_{i+1}}{\lambda^*_{i+1}}\,.\end{aligned} \tag{23b}$$

The minimization update is executed for the sequence $i = \mu+1, \mu+2, \cdots, \nu-1$, which is defined to be an iteration in the geometrical relaxation (GR) cycle. After repeating $\sim \nu - \mu$ times the iteration, the modulus of $\nabla_i\Psi$ is reduced by a considerable amount, i.e. the curve approaches the desired solution. Hence, one Geometrical Relaxation (GR) cycle consists of $\nu - \mu$ iterations, which has $(\nu-\mu)(\nu-\mu-1) \approx (\nu-\mu)^2$ minimization updates.

Observe that the vectors $\hat{\mathbf{y}}_i$ and $\hat{\mathbf{z}}_i$ are calculated only at the beginning of the minimization procedure. Since the plane over which the point $\mathbf{x}^*_i$ can move is kept constant, the possibility $\boldsymbol{\lambda}^*_i \to \mathbf{0}$ is ruled out and numerical instabilities are avoided.

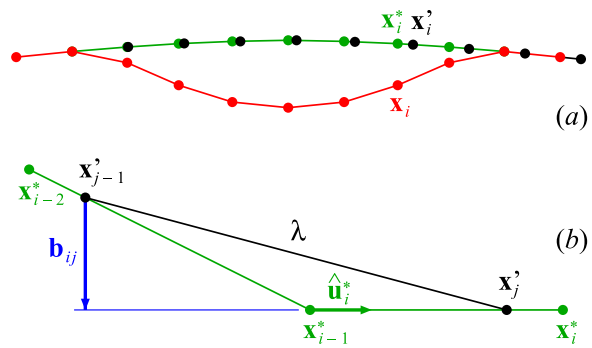

Figure 7. (*a*) *Original curve* $\mathbf{x}_i$ *(red), curve after executing the energy minimization* $\mathbf{x}^*_i$ *(green), and displaced points* $\mathbf{x}'_i$ *(black).* (*b*) *Closer view of three coordinates* $\mathbf{x}^*_{i-2}$, $\mathbf{x}^*_{i-1}$, *and* $\mathbf{x}^*_i$ *after the minimization. The unit vector* $\hat{\mathbf{u}}^*_i$ *points from* $\mathbf{x}^*_{i-1}$ *to* $\mathbf{x}^*_i$, *and the vector* $\mathbf{b}_{ij}$ *goes from* $\mathbf{x}'_{j-1}$ *to the line passing through* $\mathbf{x}^*_{i-1}$ *and* $\mathbf{x}^*_i$. *The distance between* $\mathbf{x}'_{j-1}$ *and* $\mathbf{x}'_j$ *equals* λ.

3.2.3 Point Slide. After executing the energy minimization, the point must be shifted ($\mathbf{x}^*_i \to \mathbf{x}'_i$) to restore $|\boldsymbol{\lambda}'_i| = \lambda$. Specifically, $\mathbf{x}'_i$ is displaced following the polyline to obtain $|\mathbf{x}'_i - \mathbf{x}'_{i-1}| = \lambda$ as depicted in Figure 7(a), an idea which is based on the "Follow the Leader" technique.

To find $\mathbf{x}'_j$ explicitly, consider Figure 7(b). Let $\mathbf{x}^*_{i-1}$ and $\mathbf{x}^*_i$ be two vertices in the polyline such that $|\mathbf{x}^*_{i-1} - \mathbf{x}'_{j-1}| < \lambda$ and $|\mathbf{x}^*_i - \mathbf{x}'_{j-1}| > \lambda$. Then construct the vector

$$\mathbf{b}_{ij} = \hat{\mathbf{u}}^*_i \times \left[(\mathbf{x}^*_{i-1} - \mathbf{x}'_{j-1}) \times \hat{\mathbf{u}}^*_i\right]. \tag{24}$$

The j-th coordinate is calculated with the formula

$$\mathbf{x}'_j = \mathbf{x}'_{j-1} + \mathbf{b}_{ij} + \hat{\mathbf{u}}^*_i\sqrt{\lambda^2 - |\mathbf{b}_{ij}|^2}\,. \tag{25}$$

In particular, at the beginning $\mathbf{x}'_\mu = \mathbf{x}_\mu$.

The previous displacement is performed using a linear interpolation between $\mathbf{x}^*_{i-1}$ and $\mathbf{x}^*_i$. It is not difficult to find a second order correction for the interpolated point $\mathbf{x}'_j$. This procedure is illustrated in Figure 8: the point $\mathbf{x}'_j$ is displaced in the direction of the unit vector $\hat{\mathbf{e}}^*_i$ which is perpendicular to $\mathbf{x}^*_i - \mathbf{x}^*_{i-1} = \boldsymbol{\lambda}^*_i = \lambda^*_i\hat{\mathbf{u}}^*_i$. In order to find

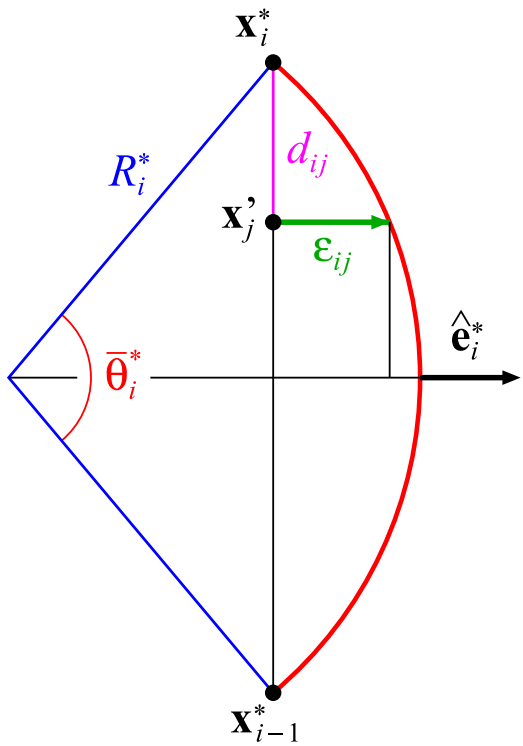

Figure 8. *Second order correction $\varepsilon_{ij}\hat{\mathbf{e}}_i^*$ to the coordinate $\mathbf{x}_j'$. The displacement is indicated by the green arrow. The arc segment has an angle $\overline{\theta}_i^*$ and a radius R_i^*. The distance between $\mathbf{x}_{i-1}^*$ and $\mathbf{x}_i^*$ is λ_i^*, and the distance between $\mathbf{x}_j'$ and $\mathbf{x}_i^*$ is d_{ij}.*

a formula for $\hat{\mathbf{e}}_i^*$, let $\hat{\mathbf{v}}_{i-}^*$ and $\hat{\mathbf{v}}_{i+}^*$ be two vectors parallel to $\hat{\mathbf{u}}_{i-1}^* \times \hat{\mathbf{u}}_i^*$ and $\hat{\mathbf{u}}_i^* \times \hat{\mathbf{u}}_{i+1}^*$ respectively. Then $\hat{\mathbf{e}}_i^*$ is chosen to point in the direction $\hat{\mathbf{u}}_i^* \times (\hat{\mathbf{v}}_{i-}^* + \hat{\mathbf{v}}_{i+}^*)$. Notice that $\hat{\mathbf{e}}_i^*$ lies in the average of the planes specified by $\hat{\mathbf{u}}_{i-1}^*$, $\hat{\mathbf{u}}_i^*$ and by $\hat{\mathbf{u}}_i^*$, $\hat{\mathbf{u}}_{i+1}^*$. But if $\hat{\mathbf{v}}_{i-}^* . \hat{\mathbf{v}}_{i+}^* \leq 0$ it is not convenient to perform the second order correction, because the curve has an *inflection* and the circumference in Figure 8 is no longer a good approximation.

To determine the length ε_{ij} of the displacement, first calculate the radius of the circumference

$$R_i^* = \frac{\lambda_i^*}{2\sin\left(\overline{\theta}_i^*/2\right)} = \frac{\lambda_i^*}{\sqrt{2 - 2\cos\overline{\theta}_i^*}} .$$

The cosine of the angle $\overline{\theta}_i^*$ can be found with the dot product $\hat{\mathbf{u}}_{i-1}^* . \hat{\mathbf{u}}_i^*$ or $\hat{\mathbf{u}}_i^* . \hat{\mathbf{u}}_{i+1}^*$. In general, these products will be different and $\cos\overline{\theta}_i^*$ is set equal to the mean value. Then the radius becomes

$$R_i^* = \frac{\lambda_i^*}{\sqrt{2 - \hat{\mathbf{u}}_i^* . \left(\hat{\mathbf{u}}_{i-1}^* + \hat{\mathbf{u}}_{i+1}^*\right)}} . \tag{26}$$

Let d_{ij} be the distance between $\mathbf{x}_i$ and $\mathbf{x}_j'$. From Figure 8 it is inferred that

$$\varepsilon_{ij} = \sqrt{(R_i^*)^2 - \left(\frac{\lambda_i^*}{2} - d_{ij}\right)^2} - \sqrt{(R_i^*)^2 - \left(\frac{\lambda_i^*}{2}\right)^2} . \tag{27}$$

Finally, the replacement $\mathbf{x}_j' \to \mathbf{x}_j' + \varepsilon_{ij}\hat{\mathbf{e}}_i^*$ is carried out. Observe that, after replacing, the modulus of the vector $\boldsymbol{\lambda}_j' = \mathbf{x}_j' - \mathbf{x}_{j-1}'$ becomes slightly different from λ. Therefore, it is necessary to move the point $\mathbf{x}_j'$ to fix the length of $\boldsymbol{\lambda}_j'$.

The second order correction is in practice very small. But it is important for points close to the surface because it avoids abrupt changes of the interaction force in the PR.

3.2.4 Cubic Spline. To select the interval to apply the GR, it is desirable to have an approximate analytical solution $\mathbf{x}(\tau)$ with boundary conditions $\mathbf{x}_\mu$, $\dot{\mathbf{x}}_\mu$, $\mathbf{x}_\nu$, and $\dot{\mathbf{x}}_\nu$. The two-dimensional static Euler–Bernoulli equation describing a beam having a small deflection υ is

$$\frac{\mathrm{d}^4\upsilon}{\mathrm{d}\tau^4} = \frac{Q}{EI} .$$

For zero transverse load ($Q = 0$) the solution is a cubic spline. The four integration constants are determined using the boundary conditions $\upsilon(\tau_\mu)$, $\dot{\upsilon}(\tau_\mu)$, $\upsilon(\tau_\nu)$, and $\dot{\upsilon}(\tau_\nu)$.

In 3D the cubic spline becomes

$$\mathbf{x}_{\mathrm{cub}} = (1-\tau)\mathbf{x}_\mu + \tau\mathbf{x}_\nu + \tau(1-\tau)\left[(1-\tau)\mathbf{s}_\mu - \tau\mathbf{s}_\nu\right] , \tag{28}$$

where $\tau \in [0, 1]$. Let $\mathbf{X}_{\mu\nu} = \mathbf{x}_\nu - \mathbf{x}_\mu$ and $\hat{\mathbf{U}}_\mu$, $\hat{\mathbf{U}}_\nu$ be two unit vectors parallel to $\dot{\mathbf{x}}_\mu$, $\dot{\mathbf{x}}_\nu$ respectively. If the vectors $\mathbf{s}_\mu$ and $\mathbf{s}_\nu$ (associated with the cubic dependencies on τ) are perpendicular to the line $(1-\tau)\mathbf{x}_\mu + \tau\mathbf{x}_\nu$ connecting the points $\mathbf{x}_\mu$ and $\mathbf{x}_\nu$, then

$$\mathbf{s}_\mu = \frac{|\mathbf{X}_{\mu\nu}|^2}{\mathbf{X}_{\mu\nu}.\hat{\mathbf{U}}_\mu}\hat{\mathbf{U}}_\mu - \mathbf{X}_{\mu\nu}$$

$$\mathbf{s}_\nu = \frac{|\mathbf{X}_{\mu\nu}|^2}{\mathbf{X}_{\mu\nu}.\hat{\mathbf{U}}_\nu}\hat{\mathbf{U}}_\nu - \mathbf{X}_{\mu\nu} . \tag{29}$$

A small deflection occurs when $\hat{\mathbf{U}}_\mu$ and $\hat{\mathbf{U}}_\nu$ are nearly parallel to $\hat{\mathbf{X}}_{\mu\nu} = \mathbf{X}_{\mu\nu}/|\mathbf{X}_{\mu\nu}|$.

3.2.5 Interval Selection. To find a suitable interval to apply the GR, the first step is to search for intervals whose end points $\mathbf{x}_\mu, \mathbf{x}_\nu$ are *close* to the surface, and whose inner points $\mathbf{x}_{\mu+1}, \cdots, \mathbf{x}_{\nu-1}$ are *far* from the surface. Specifically, a point is considered to be close (far) when the distance to the surface is smaller (larger) than 5% of the average artery diameter. It will be seen that in the PR cycle a point near to the surface can be bouncing (Section 4.4).

Next, discard intervals having few segments, say less than 5. Also exclude the tip of the WI, which is curved, and any other interval having a nonconstant flexural rigidity.

For each of the remaining intervals execute the following operations. Given $\mathbf{x}_\mu$ and $\mathbf{x}_\nu$ with tangent vectors $\dot{\mathbf{x}}_\mu = \hat{\mathbf{u}}_\mu + \hat{\mathbf{u}}_{\mu+1}$ and $\dot{\mathbf{x}}_\nu = \hat{\mathbf{u}}_\nu + \hat{\mathbf{u}}_{\nu+1}$, determine the cubic spline $\mathbf{x}_{\text{cub},i}$. Then calculate the mean square deviation

$$\sigma^2_{\mu\nu} = \frac{1}{\nu - \mu} \sum_{i=\mu}^{\nu} \sigma_i^2 \,, \tag{30}$$

where $\sigma_i^2 = |\mathbf{x}_i - \mathbf{x}_{\text{cub},i}|^2$. The cases of interest occur when the deviation $\sigma_{\mu\nu}$ is large. Moreover, the cubic spline is not a good approximation unless $\hat{\mathbf{U}}_\mu$ and $\hat{\mathbf{U}}_\nu$ are nearly parallel to $\hat{\mathbf{X}}_{\mu\nu}$; that is, a bad approximation results if $1 + \hat{\mathbf{U}}_\mu.\hat{\mathbf{X}}_{\mu\nu}$ or $1 + \hat{\mathbf{U}}_\nu.\hat{\mathbf{X}}_{\mu\nu}$ are small. Hence, calculate the following figure of merit

$$\chi_{\mu\nu} = (1 + \hat{\mathbf{U}}_\mu.\hat{\mathbf{X}}_{\mu\nu})^2 (1 + \hat{\mathbf{U}}_\nu.\hat{\mathbf{X}}_{\mu\nu})^2 \, \sigma_{\mu\nu}, \tag{31}$$

and select the interval with the largest $\chi_{\mu\nu}$.

It is not mandatory to move the points when the distance between $\mathbf{x}_i$ and $\mathbf{x}_{\text{cub},i}$ is small, so that a reduced interval can be chosen. If $\sigma_i < 0.10\,\sigma_{\mu\nu}$ for $i = \mu + 1, \mu + 2, \cdots, \mu_+$, then replace $\mu \to \mu_+$. Likewise, if $\sigma_i < 0.10\,\sigma_{\mu\nu}$ for $i = \nu - 1, \nu - 2, \cdots, \nu_-$, then replace $\nu \to \nu_-$. Note that a shorter interval decreases the PT to calculate the improved curve, which is proportional to $(\nu - \mu)^2$. Moreover, the angles $\measuredangle(\hat{\mathbf{N}}_\mu, \hat{\mathbf{U}}_\mu)$, $\measuredangle(\hat{\mathbf{N}}_\nu, \hat{\mathbf{U}}_\nu)$ are likely bigger than the angles $\measuredangle(\hat{\mathbf{N}}_{\mu+}, \hat{\mathbf{U}}_{\mu+})$, $\measuredangle(\hat{\mathbf{N}}_{\nu-}, \hat{\mathbf{U}}_{\nu-})$, where $\hat{\mathbf{N}}_i$ stands for a vector normal to the artery's surface. Hence, there is a smaller probability that the improved curve intercepts the surface when the interval is reduced.

If an interception occurs, then do not update $\mathbf{x}_i \to \mathbf{x}_i^*$ but use a linear interpolation $\mathbf{x}_i \to \zeta\mathbf{x}_i^* + (1 - \zeta)\mathbf{x}_i$ with $\zeta \in (0, 1)$. In practice, ζ should be large but it must avoid the intersection. Further, to ensure numerical stability it is convenient to limit ζ such that the tip of the WI does not displace a distance greater than λ. Thus, after executing the GR check if $|\mathbf{x}_n - \mathbf{x}'_n| < \lambda$, otherwise decrease ζ and repeat the interpolation.

3.2.6 Pseudocode.

```
void GeometricalRelaxation(void){
    6. select the interval μ < i < ν to apply the GR, see
       Section 3.2.5;
    7. execute ν − μ iterations (with a total of (ν − μ)^2
       energy minimization updates), see Section 3.2.2;
    8. shift the points x_{μ+1}, x_{μ+2}, ···, x_n to restore the
       length |λ_j| = λ, see Section 3.2.3;
}
```

Now, the PT of the GR will be analyzed. The number of operations necessary to determine the interval in line **6** is proportional to n. Let us change the resolution of the WI in such a way that $\lambda \propto 1/n$. If the shape of the WI does not vary appreciably, then the position of the points $\mathbf{x}_{\mu 1}, \mathbf{x}_{\nu 1}$ before and $\mathbf{x}_{\mu 2}, \mathbf{x}_{\nu 2}$ after changing the resolution will be nearly the same. Thus, it is concluded that μ, ν are proportional to n and the PT in line **7** scales with n^2 (see Section 3.2.5). Similarly, the PT in line **8** (proportional to $n - \mu$) scales with n. In summary, the average PT of the GR cycle is

$$t_{\text{geo}} = t_{\text{g}1} n + t_{\text{g}2} n^2 \,. \tag{32}$$

3.3 Combination of PR and GR

A major drawback of the PR is that the WI moves as rigid structure about a fixed point. Depending on the boundary conditions this can be very hard to achieve. For example, the segment $\overline{P_1 P_2}$ in Figure 9 needs to turn up but it is hindered by contact points.

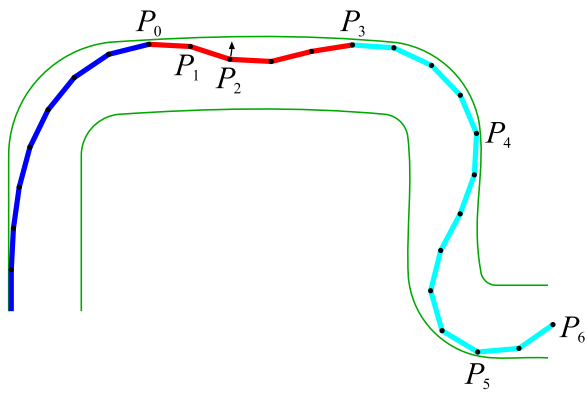

Figure 9. *WI segments inside an artery. In order to relax, the segment $\overline{P_1P_2}$ should rotate upwards about point P_1 as indicated by the arrow. Note that from P_2 to P_6 the WI is rigid, so that the resulting translation is hindered by the contact points P_3 and P_4. Nor can it move downwards because of P_5. The GR is not subjected to this restriction, since from P_3 up to P_6 the WI can slide. It is especially designed to relax intervals like from P_0 to P_3 (red).*

One possible solution is the GR developed in Section 3.2, which allows the WI to slide. The GR is executed after a PR cycle (see Figure 10) and does not interfere with it, because the GR is much faster than the PR (Section 4.3). In particular, if a user action takes place during a PR or a GR cycle, then it is interrupted and a Tip Relaxation is executed (this ensures stability). Moreover, the shape of the tip (where the actions take place) looks more natural. The combination of both techniques results in a more realistic WI behavior than using only the relaxation proposed by Konings et al. (2003).

3.4 Wire Device

Here, a simple device to capture the WI motion is described (see Figure 11). In cardiovascular procedures, the WI sweeps at most a length of 150 mm inside the coronary. In view of this fact, the required materials are as follows:

- Support box.
- Pipe tube of length 320 mm, with a small window in the middle.
- Light and opaque cylinder 170 mm long.

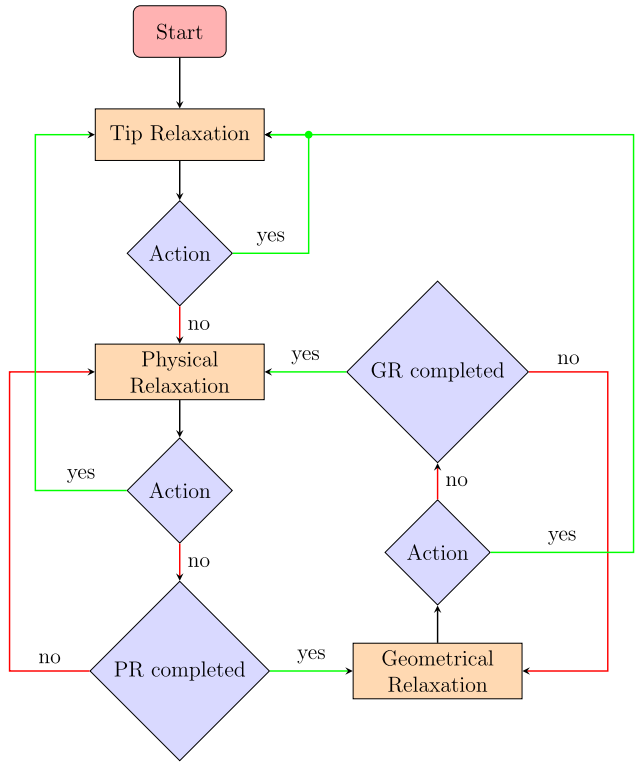

Figure 10. *Workflow. In the "Tip Relaxation" (Section 3.1) the function* `PhysicalUpdate` *is applied to the tip of the WI and also to some selected segments. When the "Physical Relaxation" is called, $\frac{1}{2}m(m+1)$ updates are executed. The PR is completed if the cycle ends; that is, after $\frac{1}{2}n(n+1)$ updates. In the same way, when the "Geometrical Relaxation" is called, $m(m+1)/(\nu-\mu)$ iterations are executed to improve the curve. The GR is completed after $\nu-\mu$ iterations.*

- Optical mouse with a precision of 1200 dpi or higher.
- Set of catheter and steerable guidewire with 150 mm free length.

The WI is attached to the cylinder, which is put inside the pipe. In particular, the friction between the pipe and the cylinder must be small. The mouse is fixed over the pipe in such a way that the light-emitting diode stays on the window. Moreover, it is possible to add extra commands to improve the simulator. For instance, the mouse buttons can simulate the contrast injection or the activation of the X-ray employed in video generation. Also, a USB-joystick with two axes can be used to change the C-arm perspective.

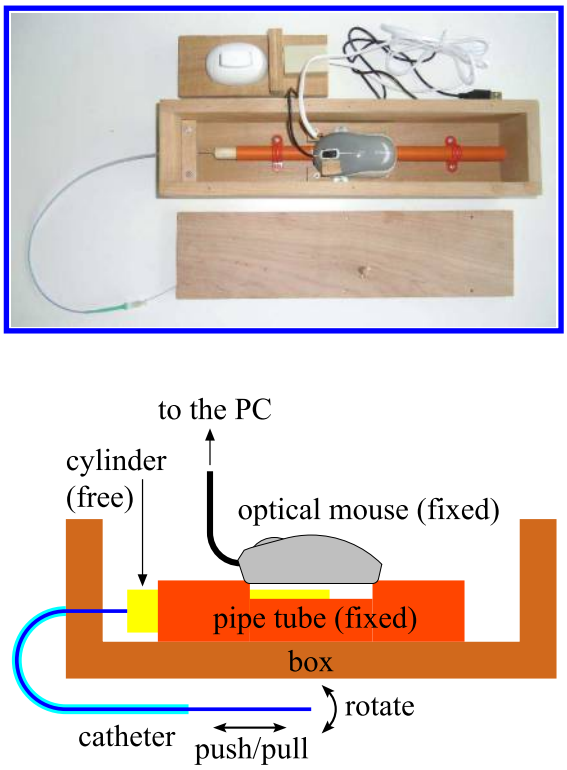

Figure 11. *Photography (top-view) and sketch (cross-view) of the WI device. The pipe has a small window and the mouse is over the window. Translating and rotating the WI also translates and rotates the cylinder, which is captured by the mouse.*

The WI movement is transferred to the cylinder and captured by the mouse according to:

- Pushing and pulling the WI = cursor up and down.
- Rotating the WI = cursor left and right.

The mouse must be aligned with the axis of the cylinder; otherwise translations and rotations will appear mixed. Depending on the mouse resolution, pointer speed, and cylinder diameter, different cursor movements are obtained. Hence, a calibration is required to provide a correct feedback to the user. As an alternative to the optical mouse, a piezoelectric captor can be connected to detect the cylinder motion.

The device has the technology of an optical mouse, whose movements can be read with basic functions in any programming language. The manufacturing cost is low and the portability allows the device to be used without platform restrictions.

Since the tip of the WI is soft, the contribution to the sense of touch is not significant. The force feedback is due mainly to the friction between the WI and the catheter (Takashima et al., 2014). In our device this force is already embodied because the WI slides inside the catheter. This removes the complex problem of coupling haptics and graphic simulation, especially because they proceed at different frequencies (of the order of 1000 Hz and 30 Hz, respectively).

4 Technical Evaluation

In order to validate the usefulness and to examine the limitations of the methods developed in this work, several analyses are performed including the stability, WI resolution, and PT of the PR and GR. Moreover, the interaction between the WI and the artery is inspected. Finally, the present model is compared with the model of Alderliesten et al. (2004).

In the simulations, a flexural rigidity EI equal to 6.35×10^{-9} Nm^2 is assumed. The algorithm was implemented in C++, and the tests were performed in a computer having a Intel Core i7-4500U (2.40 GHz) and 16 GB of RAM.

4.1 Stability Analysis

The total PT was tested for the artery shown in Figure 12, which includes a T-like and a Y-like bifurcation (Baier et al., 2015). In the first part of the simulation, the WI is outside the artery and it is quickly pushed inside (only the Tip Relaxation is applied). The result (green curve) looks unphysical, but the algorithm does not crash during a fast insertion of the WI. The stability is also verified if λ increases to 2.5 mm, so that a deeper frontal collision occurs at the T-like bifurcation. However, if the WI becomes very stiff (a huge flexural rigidity), then it will "perforate" the artery (like a needle) and the behavior becomes unstable.

In contrast, the algorithm of Alderliesten et al. (2004) demands a slow insertion of the WI; otherwise it can crash. For example, in numerical tests Konings et al. (2003) and Alderliesten et al. (2007) used an internal

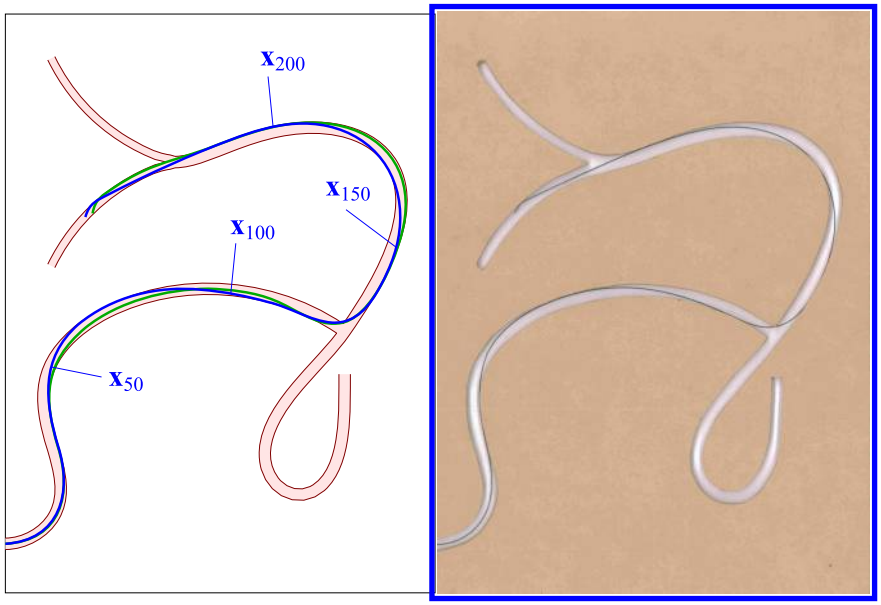

Figure 12. *Artery with a T-like and a Y-like bifurcation. (Left) The WI has 250 segments, $\lambda = 1$ mm, and it has been quickly inserted into the artery (green curve). In this part, the program executed only Tip Relaxations and the time consumed was 0.24 seconds. In the second part, no action takes place and a combination of 100 relaxation cycles (Physical and Geometrical) is executed, so that equilibrium is attained (blue curve). The coordinates indicate the location of some WI joints. (Right) Mockup representing the stiff artery. The WI inserted in the artery has the same shape as the blue curve. The average separation between the physical WI and the blue curve is 0.262 mm with a standard deviation of 0.227 mm. Hence, the calculations with the model developed in this work give a realistic result.*

stepsize smaller than $\lambda/10$. Since they insert the new segment in the proximal end of the WI, to guarantee stability they must execute at least ten times the complete relaxation cycle before a new action takes place. As in Equation 20, their PT is proportional to n^3 for large n, but in our case it is proportional to a constant plus $n^{3/2}$ (see Equation 21). Hence, this method works much faster under stress conditions.

In the second part of the simulation, a large number of cycles are executed. The result is the blue curve in Figure 12 (left) and a numerical comparison with experiment (right) shows that the calculations are truthful. Besides the specific case in Figure 12, several paths have been tested and the results were always good.

In real procedures, the physician should not insert the WI quickly, to avoid vascular damage. For security reasons, in the specific case of teleoperation the speed of the slide platform is less than 10 mm/s (Yu et al., 2015). On the other hand, one of the most annoying situations encountered by users in simulators is the time delay between the action and the response. In our simulator (green curve in Figure 12) the average speed was $(250\ \text{mm})/(0.24\ \text{s}) \approx 1\ \text{m/s}$.

4.2 Segment Size

The PT will depend on the artery's resolution and on the size of the segment λ. The method of Baier et al. (2015) to calculate $\mathbf{G}_i$ is almost independent of the artery's resolution. This artery model refers to a geometry which does not depend on time. Otherwise the proposed method is not feasible because changes of shape make it more difficult to use precomputed data structures for expediting collision tests during simulation (Brown et al., 2004).

If λ decreases but the WI length remains the same, the total number of segments n increases. Hence, with a higher WI resolution the PT becomes longer. To determine the optimal segment size (Alderliesten et al., 2004), the influence of λ on the shape of the

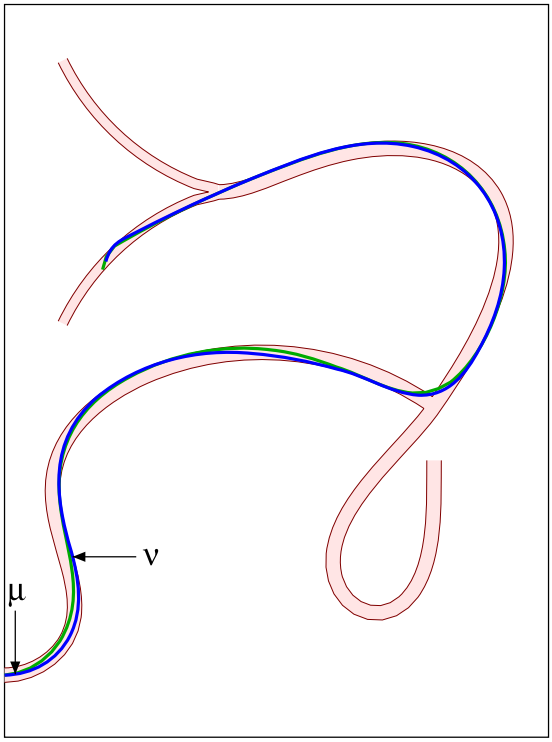

Figure 13. *The green WI_A has $n_A = 100$ segments, $\lambda_A = 2.5$ mm and the blue WI_B has $n_B = 250$ segments, $\lambda_B = 1$ mm. Hence $n_A\lambda_A = n_B\lambda_B$. The arrows indicate one of the intervals $\mu < i < \nu$ where the GR is applied. In the case of WI_A it was found that $\mu_A = 1$, $\nu_A = 13$ and in the case of WI_B it was found that $\mu_B = 2$, $\nu_B = 30$. Thus, μ and ν are closely proportional to n.*

WI must be investigated. Afterwards, set the size to the maximum value which gives a satisfactory visual effect.

In Figure 13, the simulations for $\lambda_A = 2.5$ mm (WI_A) and $\lambda_B = 1$ mm (WI_B) are compared. The equilibrium looks similar, but the time t_A required for WI_A is only 11% of the time t_B required for WI_B. The shape difference is not due to the precision of the calculations with different values of λ, but to the contact points with the artery, which is not the same in the case of WI_A and in the case of WI_B. The WI_A has less contact points and in the T-like bifurcation the WI_A penetrates deeper inside the corner of the artery wall. The WI_B has a bigger resolution and the result is closer to the real artery (see Figure 12).

Table 1. *PT of the PR (t_{phy}) and of the GR (t_{geo}) for Different Resolutions: $\lambda_A = 2.5$ mm, $\lambda_B = 1.0$ mm, and $\lambda_C = 0.4$ mm. The PT Does Not Include the Fast Insertion of the WI, but only the Relaxation between the Green and the Blue Curves in Figure 12. The Approximated Times $t_{phy,fit}$ and $t_{geo,fit}$ Have Been Obtained with Equation 33*

λ_X	2.5	1.0	0.4
t_{phy}	0.9840	9.330	103.7
t_{geo}	0.0160	0.0704	0.2431
$t_{phy,fit}$	1.026	9.321	103.7
$t_{geo,fit}$	0.0220	0.0671	0.2435

4.3 Physical and Geometrical PT

A further comparison is made using $\lambda_C = 0.4$ mm (WI_C), so that $\lambda_A/\lambda_B = \lambda_B/\lambda_C = 2.5$ or $n_B/n_A = n_C/n_B = 2.5$. The relative PT is in Table 1 and for increasing resolution the PT of the PR becomes much larger than the PT of the GR. The data can be approximated with Equations 20 and 32

$$t_{phy} = 0.716\left(\frac{n}{100}\right)^2 + 0.310\left(\frac{n}{100}\right)^3$$
$$t_{geo} = 0.01875\,\frac{n}{100} + 0.00323\left(\frac{n}{100}\right)^2 . \qquad (33)$$

From Table 1 it can be read that

- For $\lambda_A = 2.5$ mm or $n_A = 100$: $t_{phy}/t_{geo} = 61.6$
- For $\lambda_B = 1.0$ mm or $n_B = 250$: $t_{phy}/t_{geo} = 132.5$
- For $\lambda_C = 0.4$ mm or $n_C = 625$: $t_{phy}/t_{geo} = 426.5$

Note that the ratio t_{phy}/t_{geo} increases from n_A to n_B by a factor 2.15, and from n_B to n_C by a factor 3.22. These factors are close to $n_B/n_A = n_C/n_B = 2.5$ or nearly proportional to n. Indeed, for $t_{p1} = t_{p2} = 0$ in Equation 20 and $t_{g1} = 0$ in Equation 32, it follows that $t_{phy}/t_{geo} \propto n$. In general, for large n the time t_{geo} is much smaller than t_{phy}.

The PT of the GR is discussed now in detail. For a fixed n and given μ, ν, the time in Equation 32 can be put in the form

$$t_{geo} = t_{\mu\nu 0} + t_{\mu\nu 1}(\nu - \mu) + t_{\mu\nu 2}(\nu - \mu)^2 . \qquad (34)$$

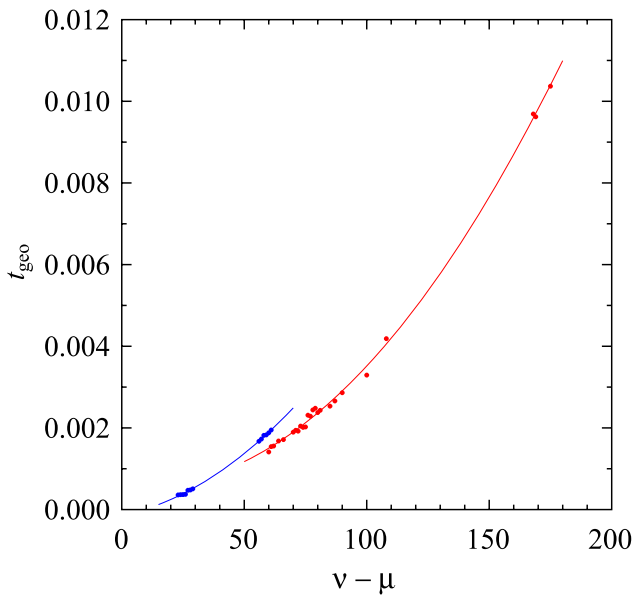

Figure 14. *GR relaxation time t_{geo} as function of the interval length $\nu - \mu$. The blue color represents the WI_B with $n_B = 250$ segments (blue curve in Figure 13) and the red color represents the WI_C with $n_C = 625$ segments (not shown in Figure 13). The points are the PT measured in numerical simulations and the lines are the fits performed with Equation 34.*

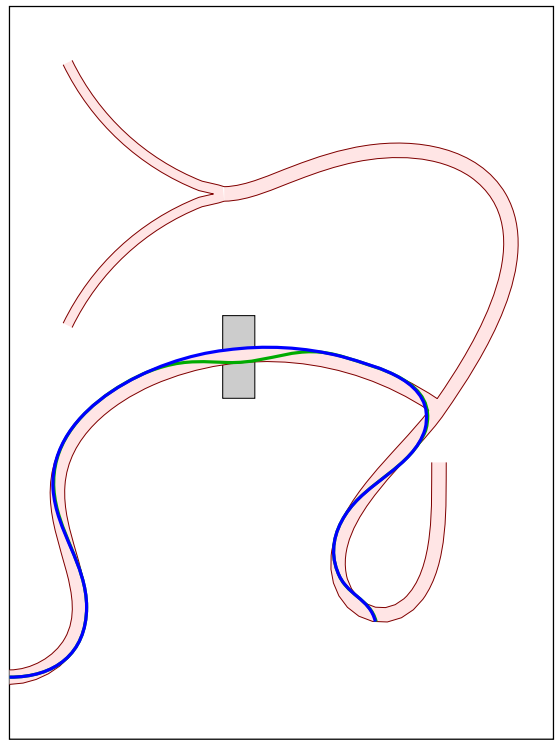

Figure 15. *Initial curve (green) and the final equilibrium curve (blue) obtained after a very long relaxation time. The final result is the same with or without the GR. The analysis is focussed in the WI portion located inside the gray box, which goes from WI segment number 90 to 95. In this interval are seen the most relevant changes during relaxation.*

The results for WI_B and WI_C are shown in Figure 14. Note that there are points missing in the numerical experiments because in the calculations not every interval size $\nu - \mu$ occurs. In particular, the blue points are not far from the red points for $\nu - \mu \approx 60$.

The blue points in the interval $20 < \nu - \mu < 30$ correspond to the red points in the interval $60 < \nu - \mu < 90$, because μ and ν are nearly proportional to n (Section 3.2.6). Also, the blue points in $55 < \nu - \mu < 60$ correspond to the red points in $165 < \nu - \mu < 175$.

The PT for a single energy minimization does not depend on the total number of WI segments. Since $(\nu - \mu)^2$ minimization updates are executed in a GR cycle, the quadratic coefficient in Equation 34 should always be the same. Indeed, this coefficient is equal to $t_{g2} = 0.003663, 0.003586$ for WI_B, WI_C, respectively, and the difference is 2%.

It is also interesting to compare the PT using the PR (case P) and using both the PR and the GR (case G). The outcomes are highly dependent on the initial WI shape and on the boundary conditions (artery geometry). For instance, Figure 15 shows an initial curve (green) and the situation is similar to that depicted in Figure 9. Although the final result is the same in cases P and G (blue curve in Figure 15), the relaxation times are very different. Specifically, the time is computed so that the difference, between the blue and green curve for the segments inside the gray box, is reduced to 10%. The result is $t_P/t_G = 3.73$, which means that the PT with GR is only 27% of the PT without GR.

As pointed out previously, the ratio t_P/t_G depends on the specific boundary conditions and on the initial WI shape. In all cases $t_G < t_P$ is obtained, but the reduction is not always noticeable. In summary, using both the PR and GR a shorter PT is achieved, although the pertinent

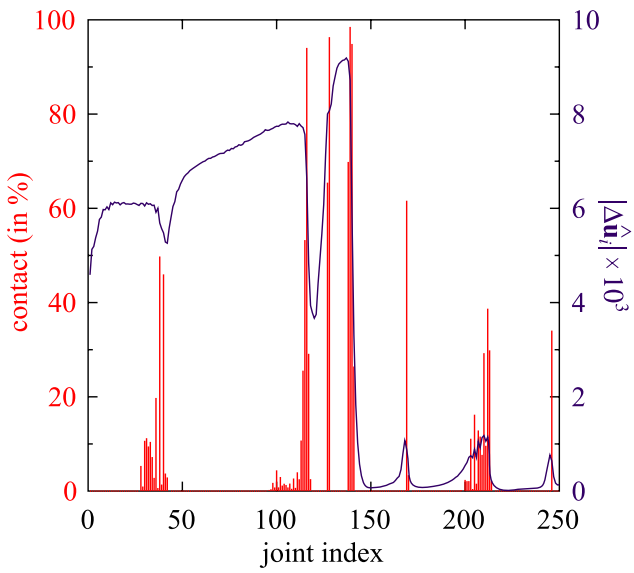

Figure 16. *The red bars represent the percentage of the time in which each joint (blue curve in Figure 12) is in contact with the artery's surface. The magenta curve represents the average modulus of the unit vector update $\Delta\hat{\mathbf{u}}_i$ during a PR cycle.*

improvement of the method is found when the WI is hindered.

4.4 Wire-Artery Contact

It will now be analyzed how much time each point is in contact with the artery in a *static solution* (see Figure 16). In general, a softer WI (small flexural rigidity EI) will have more points (a longer interval) in contact with the artery than a stiffer one (Alderliesten et al., 2007; Tang et al., 2010). Also, the shape of the artery will influence the number of collisions. Hence, the flexural rigidity and the shape affect the PT to compute the surface energy gradient in Equation 9.

Only few points are effectively touching the surface, holding the WI to the equilibrium position. The points bounce in the artery and the total number of contacts vary from one step to the next. For instance, the surface force can eject the point and then it becomes zero. In the next steps, due to the elastic restoring force of the WI, the same point can move back.

The magenta curve in Figure 16 shows the modulus of the update $\Delta\hat{\mathbf{u}}_i$. In particular, the maximum $|\Delta\hat{\mathbf{u}}_{137}| = 9.2 \times 10^{-3}$ corresponds to an amplitude variation of 4.6 μm around the average position of $\mathbf{x}_i$ for $137 \leq i \leq 250$. Note that in one complete PR cycle, the unit vector $\hat{\mathbf{u}}_i$ will be updated i times. Furthermore, after a joint collision has been surpassed, the modulus drops because the contribution of the surface gradient is suppressed from the sum in Equation 9.

Although the numerical solution looks unstable, the oscillations are tiny and they are not perceptible. Moreover, the algorithm is usually applied in dynamic simulations where the WI is moving, and a final equilibrium configuration is not required.

4.5 Comparison of Physical Models

The PR is essentially the same relaxation introduced by Alderliesten et al. (2004). The difference is that in the energy of the i-th joint $U_i = C_i g(\theta_i)$ we use the approximation $g_1(\theta_i) = (13 - 14\cos\theta_i + \cos^2\theta_i)/12$, while Alderliesten et al. (2004) use $g_2(\theta_i) = (1 - \cos^2\theta_i)/2$. Thus, in the calculations

$$\frac{k_i}{\lambda^2} = \kappa_{i-1} \lesssim 1$$

$$\frac{k_i'}{\lambda^2} = \kappa_i \lesssim 1$$

are replaced by

$$p_i \gtrsim 1$$

$$q_i \gtrsim 1$$

respectively (see Equation 8).

The functions $g_1(\theta)$ and $g_2(\theta)$ are compared with the exact $g(\theta) = \theta\sin(\theta/2)$ in Figure 17. All functions have a minimum at $\theta = 0$ and, in the absence of external forces, equilibrium is achieved when there is no bending. For $\theta < 0.1$ rad $= 5.7°$ they are almost identical: the errors of $g_1(\theta)$ and $g_2(\theta)$ are less than 4.7×10^{-5}% and 0.29% respectively. But for $\theta \sim 1$ rad $= 57°$ the function $g_1(\theta)$ is clearly superior.

Numerical simulations performed with g_1 and with g_2 have been compared. Specifically, the blue curve in Figure 13 ($\lambda_B = 1$ mm) is relaxed over a long period of time using our model (without including the GR) and using the model of Alderliesten et al. (2004). The aver-

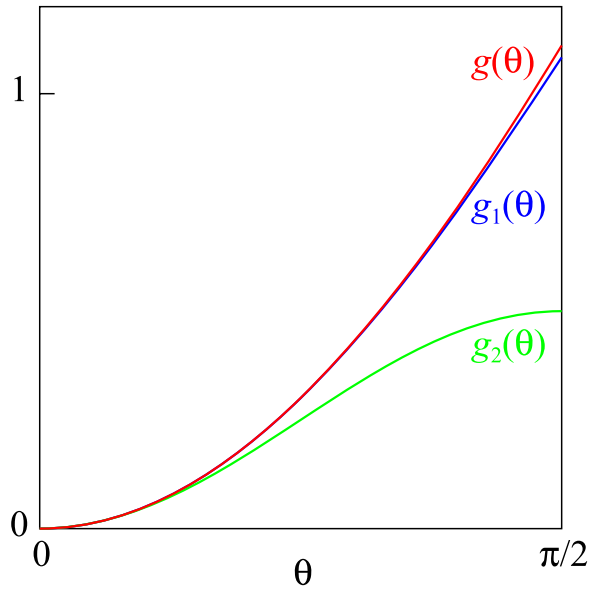

Figure 17. *Comparison of the functions $g(\theta)$ (red; exact), $g_1(\theta)$ (blue; this work), and $g_2(\theta)$ (green; Alderliesten et al., 2004) in the interval $0 < \theta < \pi/2$.*

age difference between both calculations is 0.052 mm, which is nearly the same precision of the calculations due to tiny oscillations around the equilibrium position (Section 4.4). Moreover, for $\lambda_A = 2.5$ mm and for $\lambda_C = 0.4$ mm the average differences are 0.121 mm and 0.010 mm respectively. Note that for small λ (higher resolution) the calculations are more precise.

Further, the following average and maximum values of the angle θ_i between $\hat{\mathbf{u}}_{i-1}$ and $\hat{\mathbf{u}}_i$ were obtained

- For λ_A: $\bar{\theta} = 4.7°$ and $\theta_{\max} = 13.6°$
- For λ_B: $\bar{\theta} = 1.9°$ and $\theta_{\max} = 6.7°$
- For λ_C: $\bar{\theta} = 0.75°$ and $\theta_{\max} = 2.9°$

Hence, the results with g_1 and with g_2 are practically the same because the angles θ_i are small. However, in a deep frontal collision of the WI with the artery, the angle is very large. In such situations, it is advantageous to use g_1 which gives a better approximation.

5 Conclusions

Using hardware in combination with an algorithm that responds in real time is helpful for training MIS. More physicians can be trained over longer periods of time (increasing skills) and no disposable instruments are needed (decreasing costs).

In this work, a simulation system for minimally invasive vascular interventions was presented. It consists of a simple device to capture the guidewire motion and two complementary methods to relax the WI. The physical model introduced by Konings et al. (2003) was improved. Specifically, the results are nearly the same for small beam deflections, but for larger deflections our approximation $g_1(\theta)$ is superior.

The divergence problem, when the denominator in Equation 16 becomes small or negative, was detected and solved. The updated formula in Equation 19 is simpler than Equation 11 of Alderliesten et al. (2004). Also, the algorithm does not crash when the surface gradient becomes large. Hence, the WI can be moved quickly into the artery.

The PR has some drawbacks which have been amended with the GR. The PT of the GR is proportional to n^2 and the PT of the PR is proportional to n^3. Therefore, the GR is faster, does not interfere with the PR, and helps to correct some WI distortions. Using both methods gives stable and realistic results, as seen in comparisons of experiments with numerical calculations.

In a stiff artery only few points of the WI are in contact with the surface. Although these points are bouncing, the numerical instability is not perceptible. Moreover, several other cases besides the ones shown in Section 4 (e.g., different artery shapes, rigidity levels, paths of the WI inside the mockup) have been tested and the outcomes have been similar to the previous ones.

Acknowledgments

This work was supported by PCI/LNCC, INCT-MACC, CNPq (454815/2015-8, 573710/2008-2, 290011/2008-6), and FAPERJ (E-26/170.030/2008).

References

Alderliesten, T., Bosman, P. A. N., & Niessen, W. J. (2006). Towards a real-time minimally-invasive vascular intervention

simulation system. *IEEE Transactions on Medical Imaging*, *26*, 128–132.

Alderliesten, T., Konings, M. K., & Niessen, W. J. (2004). Simulation of minimally invasive vascular interventions for training purposes. *Computer Aided Surgery*, *9*, 3–15.

Alderliesten, T., Konings, M. K., & Niessen, W. J. (2007). Modeling friction, intrinsic curvature, and rotation of guide wires for simulation of minimally invasive vascular interventions. *IEEE Transactions on Biomedical Engineering*, *54*, 29–38.

Baier, P. A., Srinivasan, L., Baier-Saip, J. A., Voelker, W., & Schilling, K. (2015). Surfaces for modeling arteries in virtual reality simulators. *IFAC-PapersOnLine*, *48*, 031–036.

Balaji, N. R., & Shah, P. B. (2011). Radial artery catheterization. *Circulation*, *124*, e407–e408.

Basdogan, C., De, S., Kim, J., Muniyandi, M., Kim, H., & Srinivasan, M. A. (2004). Haptics in minimally invasive surgical simulation and training. *IEEE Computer Graphics and Applications*, *24*, 56–64.

Brown, J., Latombe, J. C., & Montgomery, K. (2004). Real-time knot-tying simulation. *The Visual Computer*, *20*, 165–179.

Cao, D. Q., & Tucker, R. W. (2008). Nonlinear dynamics of elastic rods using the Cosserat theory: Modelling and simulation. *International Journal of Solids and Structures*, *45*, 460–477.

Coles, T., Meglan, D., & John, N. (2011). The role of haptics in medical training simulators: A survey of the state of the art. *IEEE Transactions on Haptics*, *4*, 51–66.

Duriez, C., Cotin, S., Lenoir, J., & Neumann, P. (2006). New approaches to catheter navigation for interventional radiology simulation. *Computer Aided Surgery*, *11*, 300–308.

Engum, S. A., Jeffries, P., & Fisher, L. (2003). Intravenous catheter training system: Computer-based education versus tradition learning methods. *The American Journal of Surgery*, *186*, 67–74.

Fuchs, K. H. (2002). Minimally invasive surgery. *Endoscopy*, *34*, 154–159.

Gallagher, A. G., & Cates, C. U. (2004). Approval of virtual reality training for carotid stenting: What this means for procedural-based medicine. *Journal of the American Medical Association*, *292*, 3024–3026.

Gao, Z. J., Xie, X. L., Bian, G. B., Hao, J. L., Feng, Z. Q., & Hou, Z. G. (2015). Fast and stable guidewire simulator for minimally invasive vascular surgery. *Engineering in Medicine and Biology Society (EMBC), 2015 37th Annual International Conference of the IEEE*, 5809–5812.

Kasper, D. (2015). *Harrison's principles of internal medicine* (19th edition). Columbus, OH: McGraw-Hill Education.

Kodama, H., Shi, C., Ikeda, S., Fukuda, T., Arai, F., Negoro, M., & Takahashi, I. (2012). Catheter motion capture with optical encoder at the insertion port to find the reference area of catheter insertion. *2012 International Symposium on Micro-NanoMechatronics and Human Science (MHS)*, 235–238.

Konings, M. K., van de Kraats, E. B., Alderliesten, T., & Niessen, W. J. (2003). Analytical guide wire motion algorithm for simulation of endovascular interventions. *Medical & Biological Engineering & Computing*, *41*, 689–700.

Luboz, V., Blazewski, R., Gould, D., & Bello, F. (2009). Real-time guidewire simulation in complex vascular models. *The Visual Computer*, *25*, 827–834.

Lunderquist, A., Ivancev, K., Wallace, S., Enge, I., Laerum, F., & Kolbenstvedt, A. (1995). The acquisition of skills in interventional radiology by supervised training on animal models: A three year multicenter experience. *Cardiovascular and Interventional Radiology*, *18*, 209–211.

Mori, T., Hatano, N., Maruyama, S., & Atomi, Y. (1998). Significance of hands-on training in laparoscopic surgery. *Surgical Endoscopy*, *12*, 256–260.

Moscucci, M. (ed.). (2014). *Grossman & Baim's cardiac catheterization, angiography, and intervention* (8th edition). Philadelphia: Lippincott Williams & Wilkins.

Müller, M., Kim, T. J., & Chentanez, N. (2012). Fast simulation of inextensible hair and fur. *Workshop on Virtual Reality Interaction and Physical Simulation (VRIPhys)*. Retrieved from http://matthias-mueller-fischer.ch/publications/FTLHairFur.pdf

Pai, D. K. (2002). STRANDS: Interactive simulation of thin solids using Cosserat models. *Computer Graphics Forum*, *21*, 347–352.

Przemieniecki, J. S. (1985). *Theory of matrix structural analysis*. Dover Civil and Mechanical Engineering. Mineola, NY: Dover.

Rubin, M. B. (2000). *Cosserat theories: Shells, rods and points*. Berlin: Springer.

Takashima, K., Tsuzuki, S., Ooike, A., Yoshinaka, K., Yu, K., Ohta, M., & Mori, K. (2014). Numerical analysis and experimental observation of guidewire motion in a blood vessel model. *Medical Engineering & Physics*, *36*, 1672–1683.

Tang, W., Lagadec, P., Gould, D., Wan, T., Zhai, J., & How, T. (2010). A realistic elastic rod model for real-time simulation of minimally invasive vascular interventions. *The Visual Computer*, *26*, 1157–1165.

Tsang, J. S., Naughton, P. A., Leong, S., Hill, A. D. K., Kelly, C. J., & Leahy, A. L. (2008). Virtual reality simulation in endovascular surgical training. *The Surgeon*, *6*, 214–220.

Willaert, W. I. M., Aggarwal, R., Herzeele, I., Cheshire, N. J., & Vermassen, F. E. (2012). Recent advancements in medical simulation: Patient-specific virtual reality simulation. *World Journal of Surgery*, *36*, 1703–1712.

Yu, Y., Guo, J., Guo, S., & Shao, L. (2015). Modelling and analysis of the damping force for the master manipulator of the robotic catheter system. *2015 IEEE International Conference on Mechatronics and Automation (ICMA)*, 693–697.